Department of Chemistry
University of Helsinki
Finland

Recovery of rare-earth elements from NdFeB magnets by zirconium phosphate ion exchangers

Junhua Xu

ACADEMIC DISSERTATION
To be presented, with the permission of the Faculty of Science of the University of Helsinki, for public examination in lecture hall A110, Department of Chemistry, on 31 August 2018, at noon.

Helsinki 2018

Supervisors

Adjunct Professor Risto Koivula

Honorary Professor Risto Harjula

Radiochemistry Unit

Department of Chemistry

University of Helsinki

Pre-examiners

Associate Professor Teodora Retegan

Industrial Materials Recycling

Department of Chemical and Biological Engineering

Chalmers University of Technology

Associate Professor Eveliina Repo

Separation and Purification Technology

School of Engineering Science

Lappeenranta University of Technology

Opponent

Professor Dimitrios Panias

Laboratory of Metallurgy

School of Mining and Metallurgical Engineering

National Technical University of Athens

ISSN 0358-7746

ISBN 978-951-51-4415-7 (paperback)

ISBN 978-951-51-4416-4 (PDF)

http://ethesis.helsinki.fi

Unigrafia

Helsinki 2018

I would like to dedicate this thesis for the memory of my father Mr. Qinhai Xu and my supervisor Honorary Professor Risto Harjula.

Abstract

The societal transformation from fossil fuel-based energy sources to ecologically friendly energy sources has sparked the development and utilization of electric (and hybrid) vehicles and electric generators for wind turbines, among others. Permanent magnets are essential components of these technologies.

Over the years, the production of NdFeB permanent magnets has surpassed all other kinds because of their low cost and improved magnetic properties. The rare-earth elements (REEs) Nd and Dy are critical for the production of these magnets, and they come with a significant supply risk. Also since REEs exist simultaneously in minerals, the balance problem has become increasingly evident; Nd and Dy are produced at the cost of overproduction and stockpiling of other REEs. Due to their limited life span, more and more end-of-life (EOL) NdFeB magnets have accumulated as scrap. Recycling Nd and Dy from EOL NdFeB magnets could be a more ecological means to reduce supply chain pressure and to partially solve the balance problem.

The purpose of this thesis is to develop new ion exchangers based on zirconium phosphate (ZrP) for selective recovery of Co, Nd, and Dy from EOL magnets. In general, inorganic ion exchangers, such as ZrPs, are more selective than organic resins because of the ion-sieve functionality originated from rigid structures. Two inorganic ion exchangers, crystalline alpha zirconium phosphate (α-ZrP) and amorphous ZrP (am-ZrP) and one inorganic (am-ZrP)-organic (PAN) ion exchange composite material were synthesized and characterized for their ion exchange properties in this study.

The α-ZrP was synthesized with a lower energy and acid consumption. The ion-exchange capacity from the titration result was 6.65 meq/g. Co was taken up minimally from the Co-Nd-Dy ternary solution in acidic solution (pH 1-3) when compared with the total uptake amount. The am-ZrP was synthesized by using an easy scalability synthesis method at the room temperature. The molecular formula $Zr(H_2PO_4)_{0.17}$ $(HPO_4)_{1.78}$ $(PO_4)_{0.09} \bullet 0.96H_2O$ was calculated from the results of digestion experiment, ^{31}P NMR, and TG analysis. The molecular formula suggested that the theoretical ion-exchange capacity of am-ZrP was 6.97 meq/g. The column elution study of am-ZrP utilized a stepwise gradient elution; Almost complete metal separation was achieved from a mixed 1.0 mM equimolar solution. These promising results encouraged us to apply am-ZrP to a larger lab-scale study.

To solve the possible operation problems in scale-up column separation, an am-ZrP/polyacrylonitrile composite was synthesized as bead form. X-ray tomography demonstrated a good spatial distribution of ion-exchange active component am-ZrP in the polymer matrix. Column-optimized experiments for the synthesized composite were performed by altering running temperature, speed, and concentration of the elution agent (HNO_3) as well as feed concentration and loading degree. When the column was run at lower speed and at higher temperature, the purity of metal fractions in the effluent was highly enhanced relative to the feed. Gradient elution at 50°C was adopted for metals recovery from the simulated leachate with the concentration 7.6 g/L which in total consisted of 1.4% Co, 9.3% Dy, and 89.3% Nd. Obtaining complete separation was not possible by a single column due to the high Nd concentration in the feed. It is possible to obtain pure Co at the beginning of elution but the separation of Nd and Dy was not possible due to the materials uptake preference for Dy/Nd and their concentration in the feed.

List of original publications

I Xu J, Wiikinkoski EW, Koivula R, Zhang W, Ebin B, Harjula R, 2017, HF-Free Synthesis of α-Zirconium Phosphate and Its Use as Ion Exchanger for Separation of Nd(III) and Dy(III) from a Ternary Co–Nd–Dy System*, Journal of Sustainable Metallurgy*, 3(3), 646-658.

II Xu J, Koivula R, Zhang W, Wiikinkoski EW, Hietala S, Harjula R, 2018, Separation of cobalt, neodymium and dysprosium using amorphous zirconium phosphate*, Hydrometallurgy*, 175, 170-178.

III Xu J, Virolainen S, Zhang W, Kuva J, Sainio T, Koivula R, 2018, Polyacrylonitrile-encapsulated amorphous zirconium phosphate composite adsorbent for Co, Nd and Dy separations, *Chemical Engineering Journal*, 351, 832-840.

The author contributions to the publications:

The author carried out all the experimental and analyses work together with co-authors. The author drafted all manuscripts I-III.

In article I, the author carried out all experiments and characterizations.

In article II, the author performed all experiments and characterizations, except the digestion experiment and ^{31}P NMR.

In article III, the author completed all the experiments and characterizations, except the SEM and X-ray Tomography imaging, and the intraparticle diffusion modeling.

List of abbreviations

α-ZrP	Alpha-zirconium phosphate
β	The degree of dissociation
am-ZrP	amorphous-zirconium phosphate
c_{eq}	The metal concentration in the batch stripping solution at equilibrium
DMF	Dimethylformamide
$\overline{E_M}$	The cationic equivalent fractions of M in the exchanger phase.
FT-IR	Fourier transform infrared spectra
HDDs	Computer hard disk drives
K_a	The acid dissociation constant
K_d	The distribution coefficient
K_1	The rate constants of the pseudo first-order
k_2	The rate constants of Pseudo-second-order kinetic models
MP-AES	Microwave plasma-atomic emission spectrometer
NdFeB	Neodymium-iron-boron
PAN	Polyacrylonitrile
Q	The capacity of the ion exchanger
q_e	The solute concentration in the sorbent phase at equilibrium
q_i	The rate constants of The initial amount of M loaded in the sorbent
q_M	The metal M ion equilibrium concentration in sorbent
q_t	The solute concentration in the sorbent phase at any given time t
R	Correlation coefficients
REEs	The rare-earth elements
SEM	Scanning electron microscopy
SF	Separation factor
^{31}P MAS NMR	^{31}P magic angle spinning nuclear magnetic resonance
TG	Thermogravimetry
XRD	X-Ray Powder diffraction
Z_M	The charge of M ion

Acknowledgements

The work in the thesis was performed at the University of Helsinki from 2014-2018. The work was funded by the European Rare Earth Magnet Recycling Network (EREAN) project of the FP7 Marie Curie Actions of European Commission and Chemistry Molecular Sciences Doctoral School (CHEMS) of the University of Helsinki.

I would like to thank my supervisor Honorary Professor Risto Harjula. I greatly appreciate you accepted me as your PhD student in Belgium after interview. Your trust and guidance encouraged me to be a better researcher and a person with international view. Thank you for your teaching on the chemistry knowledge, experimental skills and paper writing as well as European culture, the travel and social. Your belief motivated me using my knowledge to make the world better. I deeply respect you that you are not only the knowledgeable chemist, but also a kind, optimistic, humorous and friendly person. I will always remember you as a respectable supervisor and friend.

I would like to acknowledge my supervisor adjunct professor Risto Koivula. Thank you for your supervision, patience and constant support in my PhD study career. Your continuous comments, teaching, and encouragement was leading to my progress from one breakthrough to another. Without your help and guidance, I cannot imagine how I could have solved so many problems during my PhD research and study. Thank you for your great support on my interesting point, so I can have the opportunity to get to continually improved in column separation research. I very much appreciate your kindness, encouragement and friendship.

I would like to express my thanks to Professor Tuomo Sainio for your supervision on the column separation experiments in University Lappeenranta of Technology. I very much appreciate your help, comments and support. Thank you Sami Virolainen and Jari Heinonen.

I would like to thank Professor Jukka Lehto and university lecturer Marja Siitari-Kauppi for your support through my whole PhD study. Your encouragements motivated me to overcome many difficulties.

I would like to acknowledge Associate Professor Anu Airaksinen as custos. Thank you for your suggestions and help.

I would like to thank Professor Koen Binnemans, Peter Tom Jones and Rabab Nasser. I am grateful to all the training, networking, comments and encouragements from you all. Thanks to the EREAN

projects which offered me not only excellent research trainings and but also more international experiences.

I would like to acknowledge Professor Christian Ekberg for your teaching on solvent extraction in University Chalmers of Technology. I am grateful for the help from Professor Britt-Marie Steenari, Stefan Allard, Brucak Ebin, Marino Gergorić, Mikhail Tyumentsev, Artem Matyskin and Lovisa Bauhn.

I sincerely thank the senior project leader Jan Luyten for the training on industrial column separation in Umicore, Belgium. Thanks for the help from Elien Haccuria and Tom Smolders.

I would like to thank Associate Professor Teodora Retegan and Associate Professor Eveliina Repo for reading this thesis. Thank you for your suggestions and comments.

Thanks to my colleagues from the ion-exchange research group: Elmo, I am very grateful to work with you together that you taught me how to do the ion-exchange experiments and column operation in theory and practice. Wenzhong, how lucky I have the opportunity to meet you especially in the same office. I very much appreciate your kind and continous help and support. Thanks to my officemate Satu Meriläinen and our ion-exchange group friends Ilkka, Valtteri, Leena, Esa and Sanna. Thanks for all your contributions to my PhD studies. I am grateful to Xiaodong's friendship and help. Thank you Mikko, Jussi, Jusso, Jukka K., Sanjeev and all our colleagues in the radiochemistry unit. I cannot have so colourful life without you all in the past four years.

I also would like to express my gratitude to many excellent people for their help in the past four years. I would like to give my special thanks to Li Chen, Zhijun Yang, Yuhang Gao, Jian Lin and Jinqiu Qian from the Embassy of China in Finland for the great support. I am grateful to Chinese scholars Yuwei Chen, Hongbo Zhang, Zhipei Sun, Nan Hui, Jing Tang, Li Tian, Xiaopeng Wu and Yongdan Li for the trust and support. I would like to acknowledge all friends in CASTF for the tremendous support as well as the joys, pains and all experiences together. Zhongmei Han, Chao Zhang, Hangzhen Lan, Ming Guo and Jingwen Xia, I will remember the friendship in Kumpula campus forever.

Finally, I am very grateful for the ultimate support from my family. Thanks for my mother's pray, my uncle and my brothers' help as well as my wife's companionship, encouragement and support.

Helsinki 2018

Junhua Xu

Table of Contents

1 Introduction

Rare-earth elements (REEs) play an essential role in high technology and green industry due to their extensive use in applications such as permanent magnets, catalysts, rechargeable batteries, and lamp phosphors. Recovery and separation of REEs has become an important topic to reduce the pressure of increasing demand for these elements.

In general, NdFeB magnets consist of 30% to 40% REEs, with Nd accounting for the main component (15-30%). In addition, minor elements such as Dy and Co are added whenever special applications are needed. As such, recycling Nd, Dy, and Co from the end-of-life NdFeB permanent magnet is an important supplement for the primary production of REEs. It should be noted that REEs possess similar physical and chemical properties, which leads to difficulty in separating one from another.

Currently, environmentally friendly approaches with low cost and high efficiency are preferable in the metallurgy industry. Ion exchange technology has been extensively utilized in purification, separation and recovery of metals in chemical, food and pharmaceutical industries. Presently, it is still used industrially to produce high purity REEs. Inorganic ion-exchangers are more selective than organic resins because of the ion sieve functionality from rigid structures. So far, inorganic ion-exchangers have been used in large scales in water purification and removal of radionuclides from nuclear waste effluents.

The goal of this thesis was to develop a green separation and recovery process for REEs from NdFeB magnet leachates using zirconium phosphate (ZrP) ion exchangers. ZrPs have been extensively studied due to its high Brønsted acidity, high thermal and chemical stability and good stability under ionizing radiation. The alpha-ZrP (α-ZrP) with a layered structure and amorphous-ZrP (am-ZrP) owning a larger specific surface are worthy to be tested for the metals separation study. For the column separation, the gradient elution process has been proved as an efficient mean for materials separations. For the materials under study, the gradient elution process might be the preferred approach to obtain pure individual Co, Nd, and Dy.

2 Background

2.1 Rare-earth elements

2.1.1 Basic properties of rare-earth elements

The rare-earth elements (REEs) consist of 17 chemically similar elements, namely the lanthanide elements (Z=57-71, La-Lu) plus Sc and Y [1]. As members of the group 3 elements, they share the same typical oxidation state (+3). Certain REEs also present +2 and +4 oxidation states (e.g. Eu^{2+}, Ce^{4+}) due to half or full filling of an electron subshell.

Due to their different atomic numbers, REEs are typically separated into two subgroups, the 'light' REEs (lanthanides from La to Sm) and the 'heavy' REEs (Gd to Lu as well as Y; Eu can be considered either a light or heavy REE) [2]. The term 'rare earth' is derived from the historical difficulties of separation and obtaining high purity rare-earth metals and compounds. In reality, REEs are comparatively abundant in the earth's upper crust; for example, Ce is as abundant as Cu. Nevertheless, REEs are almost always found together in minerals [3].

Electron configurations are of critical importance and determine the chemical and physical properties of REEs. Lanthanum, cerium, and gadolinium possess $[Xe]4f^n6s^2$ electrons, while the remaining lanthanide elements possess electron configurations of $[Xe]4f^{n-1}5d^16s^2$. Scandium and yttrium show chemically similar properties due to their $(n-1)d^1ns^2$ configuration for the outermost electron shells, even though they do not have any 4f electrons [4].

In contrast to most other elements, the ionic radii of lanthanide elements continuously decrease with increase in atomic number (Figure 1a). This abnormal phenomenon is called the 'lanthanide contraction'. This is explained by the imperfect shielding of one electron by another in the same subshell [5]. Compared to the shielding effect of 4f electrons of the lanthanide ions (Ln^{3+}), the atomic radius of the lanthanide atoms is not much affected by the lanthanide contraction.

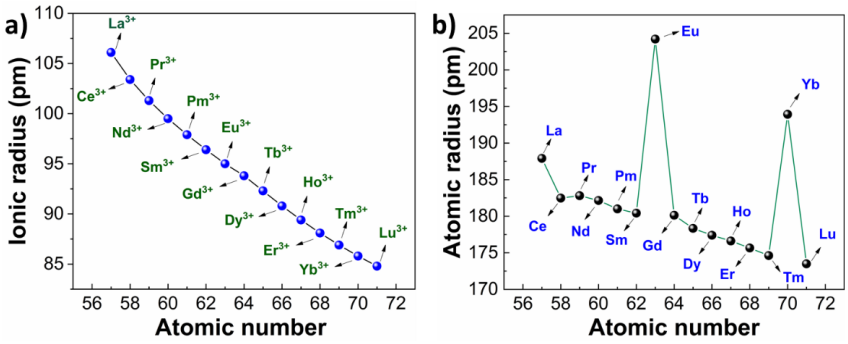

Figure 1. The lanthanide contraction. a) Ionic radius (Ln^{3+}), b) Atomic radius (Ln) [4]

The lanthanide contraction results in regular changes in properties. One of the important properties is basicity (alkalinity), which decreases with increase in atomic number.

$La^{3+}>Ce^{3+}>Pr^{3+}>Nd^{3+}>Pm^{3+}>Sm^{3+}>Eu^{3+}>Gd^{3+}>Tb^{3+}>Dy^{3+}>Ho^{3+}>Er^{3+}>Tm^{3+}>Yb^{3+}>Lu^{3+}$

The basicity variation of the lanthanide elements provide the possibilities for separating the REEs from each other in hydrometallurgy [6].

2.1.2 Challenges of REE supply and recycling

Because of their distinctive electron features, REEs possess unique magnetic, electrical, catalytic, and optical properties [3, 7]. These properties make REEs essential components in various applications, such as high-temperature superconductors, secondary batteries, and hybrid cars [8]. REEs currently play a significant role in the transition from traditional to green economy. Consequently, the demand for REEs has significantly increased. The main driving forces behind the demand surge are the applications of REEs in permanent magnets, lamp phosphors, catalysts, and rechargeable batteries [9]. In accordance with the increasing demand for REEs, the yearly global demand for rare-earth metals was estimated to be 210,000 metric tons in 2015. However, the global primary mining production of rare-earth metals was 110,000 metric tons in 2015 [8].

REEs have been classified as the highest supply risk and as the most critical raw materials by the European Commission in both 2010 and 2017 [10]. Due to their applications in green technologies, demand for Nd and Dy has been estimated to increase by 700% and 2600%, respectively, over the next 25 years [11].

To address the supply pressure of REEs, the following three approaches have been proposed: developing less critical metals to substitute for critical REEs and investing in primary mining and recycling of REEs from urban and industrial wastes [9, 12, 13]. There are two kinds of substitution methods, such as substituting REEs with common base metals and substituting critical REEs with less critical ones (for example, using more La and Ce to replace Nd and Dy). This can partially solve the 'balance problem' [14]. This refers to the balance between the economic market demand and the natural abundance of REEs in ores [15, 16]. Primary mining is an efficient way to mitigate the supply risk of REEs, but can result in a higher environmental footprint and cause the balance problem [16-18]. Recycling REEs from urban and industrial wastes is one of the strategies encouraged by the green economy towards solving both the supply risk and the balance problem.

Although recycling of REEs has been extensively studied at the laboratory scale, the application of commercial recycling of REEs is insufficient. Regarding urban mining, it is estimated that at most 1% of REEs were recycled in 2011. This was due to inefficient collection, technology obstacles, and lack of motivation [19, 20].

2.1.3 Recycling REEs from permanent magnets

Neodymium-iron-boron alloys (NdFeB magnet) are the most common REE magnets. To suit various applications, the chemical composition has to be tuned by adding minor elements (Table 1). NdFeB magnets are widely used in wind turbines, hybrid and electric vehicles, computer hard disk drives (HDDs), household electrical appliances, and many small consumer electronic devices.

Table 1. Function of the added elements in NdFeB magnets

Elements	Functions	Reference
Dy, Tb	Enhances anisotropy, coercivity, and demagnetization temperature	[9, 21]
Gd	Improves temperature efficiency	[22]
Nb	Gran refining	[22]
Co	Improves corrosion resistance	[21]
Cu, Al	Enhances sintering of the magnet alloy	[22]
Ga	Improves intrinsic coercivity and high temperature tolerance	[22]

It is estimated that approximately 26,000 metric tons of rare-earth metals have been consumed annually in the production of NdFeB magnets [13]. Due to lifecycle limitations, more and more end-of-life (EOL) magnets have accumulated, pending further treatment and recycling (Table 2). NdFeB magnets contain approximately 31 to 32 wt-% REEs. The main component is Nd, and small mixtures of Pr, Dy, Gd and Tb as well as other REEs are present for different applications. With increasing accumulation, more long-term efforts should be focused on REE recycling from EOL magnets. At the same time, improvements are needed in the development of technology and infrastructure [23]. By the year 2100, supply from recycling is estimated to fulfil half of REE demand [24]. Recycling REEs recycling is increasingly important not only as a supplement for REE demand but also as a more sustainable means of using natural resources [22].

Table 2. Present and future recycling of NdFeB magnets [9]

Permanent NdFeB magnets (Nd, Dy, Tb, Pr)	Contribution to recycling (present/future)
Hard disk drives	Decreasing
Consumer electric and electronic devices	Stable
Automobiles	Stable
Electric vehicle and hybrid electric vehicle motors	Increasing
Wind turbine generators	Increasing

Many methods have been developed for recycling REE magnets, such as direct reuse, reprocessing, hydrometallurgical methods, and pyrometallurgical methods. The advantages and disadvantages of each method are compared and explained below.

Direct reuse in its current form is the most economical means of REE magnet recycling. This is due to low energy input and the fact that chemical consumption is not necessary and no waste is generated. However, direct reuse is only applicable to large and easily accessible magnets, such as wind turbines, large electric motors, and generators in hybrid and electric vehicles [9, 13, 25, 26].

Reprocessing of alloys to magnets after hydrogen decrepitation is particularly suitable for HDDs, as less energy input is required than metallurgical methods and no waste is generated. However, mixed scrap feed and oxidized magnets are not applicable for this method. Sufficient hydrogen access is the key factor for this technology [27, 28].

Hydrometallurgical methods, including leaching, separation and precipitation processes, consist of the same processing steps as the procedures for REE production from minerals. These methods are applicable to all types of magnets. However, these methods require multi-step processing, the consumption of large amounts of chemicals, and generate excessive amounts of waste effluents [8, 9, 22].

Pyrometallurgical methods include liquid-phase processing and gas-phase extraction. These methods consist of directly melting REE magnets to obtain master alloys, which can be generally applied to all types of magnets. Compared with hydrometallurgy methods, no wastewater is generated and fewer processing steps are necessary for pyrometallurgical methods [29, 30].

For liquid-phase processing, the methods require greater energy input and large amounts of solid waste are generated by electrical refining and by the glass slag method. In addition, oxidized magnets are not suitable for direct melting and liquid-metal extraction [9].

Gas-phase extraction can be applicable to non-oxidized and oxidized alloys. Nevertheless, the consumption of chlorine gas and generation of corrosive aluminium chloride are the disadvantages of this method [22].

2.2 Hydrometallurgical method for the recovery of REEs

Hydrometallurgy is a traditional technique in the field of extractive metallurgy and uses aqueous chemistry. It has been extensively adopted industrially for the recovery of metals from ores, concentrates, and residual materials [31, 32]. Hydrometallurgy is also the traditional method for recycling REEs from permanent magnets [33]. The key procedures are leaching and separation (solvent extraction, ion exchange, or precipitation). The final product is obtained by conversion to REE fluorides or oxides (Figure 2) [34, 35].

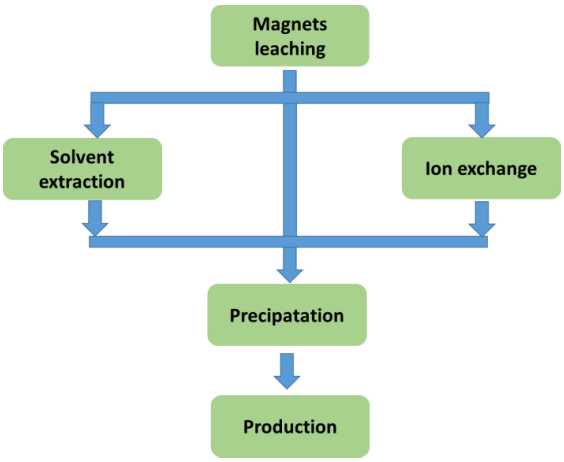

Figure 2. Key procedures of the hydrometallurgical method

In commercial separation, mineral acids are applied to dissolve EOL REE magnets to obtain the pregnant leaching solution (containing for example chloride, nitrate, and thiocyanates). Leaching NdFeB magnets is challenging as these magnets contain approximately 72 wt-% iron. Recently, a combined pyrometallurgical and hydrometallurgical method using sulfate or nitration and calcination processes followed by water leaching was developed. More than 95% REEs can be extracted and Fe (less than 1%) and other impurities remains in the solid residue [34, 35]. Electrochemical processes are also useful for selective leaching. More than 95% REEs are extracted followed by membrane electrolysis. All iron was removed by oxidization in the anolyte and subsequently precipitated as $Fe(OH)_3$ [17].

2.2.1 Solvent extraction

Solvent extraction is the classic method to separate materials (metal complexes and organic compounds) from the mixture according to the two different immiscible liquids, normally aqueous solution and organic solvent [36]. The leachate is subjected to a solvent extraction process for REE separation. The REEs from an aqueous solution are transferred to the organic phase after the formation of complexes using a selective extractant. Cationic, anionic, and solvating extractants are frequently used, such as di-(2-ethyl-hexyl) phosphoric acid (HDEHP), 2-ethylhexyl phosphoric acid-2-ethylhexyl ester (EHEHPA), 2-Ethylhexyl 2-ethylhexyphosphonic acid (PC88A), bis/2,4,4-trimethylpentyl/phosphinic acid (Cyanex 272), Tri-*n*-butyl phosphate (TBP), and

tricaprylylmethylammonium chloride (Aliquat 336) [37-39]. Representative extractants and extraction mechanisms are shown in Table 3.

Table 3 Representative extractants and extraction mechanism for REEs.

Type	Representative extractants	Extraction mechanism	Reference
Cationic extractants	HDEHP, EHEHPA, PC88A	$Ln^{3+} + +3\overline{HA} \leftrightarrow \overline{LnA_3} + 3H^+$	[40-42]
Anionic extractants	$R_3CH_3N^+ X^-$ (R: C8-C12, X: nitrate or thiocyanate)	$[R_4N{\cdot}NO_3]_{org} + Ln^{3+} + 3[NO_3^-]_{aq} \leftrightarrow [R_4N \cdot Ln(NO_3)]_{org}$	[43]
Solvating extractants	TBP	$3[TBP]_{org} + Ln^{3+} + 3[NO_3^-]_{aq} \leftrightarrow [Ln(TBP)_3(NO_3)_3]_{org}$	[44]

Due to the very similar physical and chemical properties, the selectivity of adjacent lanthanides is not very satisfactory. At industrial scale, decent separation is achieved often by using hundreds of mixer-settler units and adopted complicated flowsheets with reflux [8]. In addition, solvent extraction often involves the use of toxic volatile organic solvents. Thus, new extractants or new extraction systems are needed for REE recycling [45-47].

After the solvent extraction process by several stages of mixer-settlers, the low concentration leachate is suitable for recycling by ion-exchange technologies from a recycling efficiency and economic perspective [48, 49].

The problems described above drives the development of environmentally friendly separation methods that eliminate redundant processing units and the use of organic solvents.

2.2.2 Ion exchange

Ion exchange has played a significant role in the progress and development of purification and separation industry. Ion-exchange techniques are not only applied for purification processes, but are also extensively used in separation and extraction processes in the chemical, petrochemical, food, power, and pharmaceutical industries. Ion-exchange techniques in particular are used industrially to produce high-purity REEs [50, 51].

REE separation by ion exchange was initiated to separate fission products from nuclear reactors. With the support of the Manhattan project, ion exchange on organic resins was adopted to separate REEs and actinides [52, 53]. Theoretical analysis of column-separation processes and its pilot-scale separations has been systematically studied at the same time [52-55]. Since then, separation and purification of REEs by ion exchange replaced tedious fractional crystallization [56]. Before the 1960s, ion exchange was the dominant technology for obtaining individual REEs. Even though solvent extraction gradually became the key method for industrial production, ion-exchange technology is still widely implemented industrially to produce high-purity REEs [3, 51].

Inorganic ion exchangers are generally much more selective than organic resins due to the ion sieve functionality from the nanoporous, ordered, and rigid structures [57]. Inorganic ion exchangers are typically hydrous oxides (ZrO_2, SnO_2, $HSbO_3$, and Mn_xO_y), layered compounds (zirconium phosphates and layered double hydroxides), and framework structures that contain cavities or tunnels (zeolites, clays, pharmacosiderites, and ammonium molybdophosphate and sodium titanium silicates) [51, 58-62]. Thus far, inorganic ion exchangers have been used at large scale only for water purification and removal of radionuclides from nuclear waste effluents [63, 64].

2.3 Zirconium phosphate as inorganic ion exchanger

Zirconium phosphates (ZrPs) have received extensive attention because of its unique properties, including high Brønsted acidity, high thermal and chemical stability, and good stability under ionizing radiation. Therefore, ZrPs have found wide applications as catalysts [65, 66], ion exchangers [67-71], acid solids [72], intercalation hosts [73-75].

Alpha-zirconium phosphate, $Zr(HPO_4)_2{\cdot}H_2O$ (α-ZrP), is one primary crystalline acid salt of zirconium [76]. α-ZrP was first synthesized by Clearfield using a refluxing method and its structure was solved in the 1960s [77]. The compound $Zr(HPO_4)_2{\cdot}H_2O$ exhibits a layered structure (Figure 3). The layers are constructed by zirconium atoms connected by the oxygen atoms of the phosphate groups. Three oxygen atoms of each phosphate group bond Zr atoms, leaving one –OH group extending into the interlayer space. Adjacent layers are located as the staggered way to form a network resembling a hexagonally shaped cavity. The water molecule is situated in the cavity formed by three P–OH groups. The distances of interlayer space and between P–OH groups are 7.6 Å and 5.3 Å, respectively. The layers are held together by van der Waals forces [69, 78, 79].

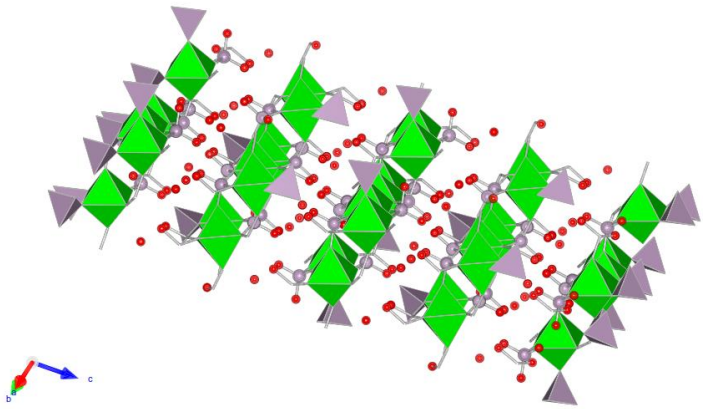

Figure 3. Polyhedral representation of the structure of crystalline α-ZrP. [ZrO_6] (green octahedron), [PO_4] (grey tetrahedron), O (grey sphere) and OH (red dot) are shown.

Representative of inorganic ion exchangers, the primarily importance of ZrP is acid stability, reasonably high ion-exchange capacity, and selectivity for specific ions [78]. The ion-exchange capacity α-ZrP is reported as 6.64 meq/g [69]. The ion-exchange behaviour of ZrP is significantly affected by its degree of crystallinity [80]. Amorphous ZrP (am-ZrP, also called semicrystalline) includes extremely small particles with a layered structure, and is observed often with a weak broad X-ray diffraction [80, 81]. The am-ZrP appears to have large amounts of microspores and possesses a comparatively greater specific surface area than that of crystalline α-ZrP [82, 83]. These unique advantages of am-ZrP enhance its function in ion exchangers, catalysts, and adsorbents [82, 84]. However, to the best of our knowledge, extremely limited studies were conducted before this work for the separation of REEs by ZrP materials.

2.4 Organic-inorganic ion exchange composite

ZrPs display excellent ion-exchange properties. However, the powdery form of ZrPs easily causes pressure build-up and clogging in fixed bed columns.

To overcome these limitations, a porous composite bead has been developed by embedding the inorganic ion exchanger into porous granulated carriers [85, 86]. Commonly used porous granulated carriers include mesoporous silica, zeolite, activated carbon, alginate, diatomite, cellulose, and porous polymers [87-95].

Polyacrylonitrile (PAN) with a linear formula $(C_3H_3N)_n$ is known as a common polymer carrier. PAN possesses excellent physicochemical properties, such as good performance on bead formation, strong adhesive force with inorganic materials, good solubility in organic solvents, high thermal stability, good radiation stability, and good chemical stability in strong acids (dissolves when the concentration exceeds 8 M HNO_3, 5 M H_3PO_4, or 5 M H_2SO_4) [96].

The composite's hydrophilicity, porosity, and mechanical strength can be modified by using a PAN-based organic binding polymer. For the PAN-inorganic composite, inorganic materials existed as the ion exchange active component. The inorganic materials can be dispersed in the polymer with a very wide range, from 5 to 90 wt-% for the different demands [97]. Due to the advantages of the PAN-inorganic composite, this kind of composite based on PAN has been extensively applied in radiochemistry, heavy metal removal, separation, and other applications [87, 98-101].

2.5 Ion-exchange theory

α-ZrP and Nd^{3+} are shown as an example to explain the ion-exchange process between metal ions and ion-exchanger ZrPs. The reaction can be expressed as

$$3\ \text{ZrP-OH} + Nd^{3+} \leftrightarrow (\text{ZrP-O})_3Nd + 3H^+ \qquad (1)$$

The distribution coefficient (K_d) represents the distribution of solute ions (Nd^{3+}) after the equilibrium between the solution and the ion exchanger (α-ZrP):

$$K_d = \frac{\left[\overline{Nd^{3+}}\right]_{eq.}}{[Nd^{3+}]_{eq.}} \qquad (2)$$

where $\left[\overline{Nd^{3+}}\right]_{eq.}$ is the concentration of Nd^{3+} taken up by α-ZrP at equilibrium (mmol/g) and $[Nd^{3+}]_{eq.}$ is concentration of Nd^{3+} remaining in solution after equilibrium (mmol/L).

In a typical batch ion-exchange experiment, α-ZrP (mass m) is placed in REE solution (volume V) and rotated until equilibrium. The K_d for Nd^{3+} can be expressed as

$$K_d = \frac{\left[\overline{Nd^{3+}}\right]_{eq.}}{[Nd^{3+}]_{eq.}} = \frac{[Nd^{3+}]_{in.} - [Nd^{3+}]_{eq.}}{[Nd^{3+}]_{eq.}} \times \frac{V}{m} \qquad (3)$$

where $[Nd^{3+}]_{eq.}$ is the concentration of Nd^{3+} remaining in the solution after equilibrium (mmol/L) and $[Nd^{3+}]_{in.}$ is the initial concentration of Nd^{3+} (mmol/L).

In equilibrium state, the selectivity coefficient is defined as the ratio of ions in solution to ions on the ion exchanger. For the exchange between the metal ions (Nd^{3+}) and hydronium ions (H^{+}), the selectivity coefficient can be calculated by

$$K_{\mathrm{Nd}/\mathrm{H}} = \frac{\left[\overline{\mathrm{Nd}^{3+}}\right]_{eq.}[\mathrm{H}^{+}]^{3}}{[\mathrm{Nd}^{3+}]_{eq.}\left[\overline{\mathrm{H}^{+}}\right]^{3}} \quad (4)$$

When sorption mechanism and system are unclear, simpler terminology has usually been used in practical ion-exchange studies. Thus

$$\left[\overline{\mathrm{M}}\right] = q_{\mathrm{eq}} \quad (5)$$

$$[\mathrm{M}] = C_{\mathrm{eq}} \quad (6)$$

Here $\left[\overline{\mathrm{M}}\right]$ (and q_{eq}) and $[\mathrm{M}]$ (and C_{eq}) are the metal concentrations in the ion exchanger and in the solution at equilibrium state, respectively. The indirect measurement was adopted for the uptake by ion exchanger. The metal concentrations are acquired by means of the changes of solution. Therefore

$$\left[\overline{\mathrm{M}}\right] = (C_0 - C_{\mathrm{eq}}) \times \frac{V}{m} \quad (7)$$

$$\left[\overline{\mathrm{H}}\right] = \mathrm{Q} - Z_{\mathrm{M}}\left[\overline{\mathrm{M}}\right] \quad (8)$$

where Q represents the total ion-exchange capacity, or how many cations can be taken up in total (milliequivalent per gram, meq/g). Z_{M} is the ion charge of M.

Equivalent fractions or mole fractions are usually used to replace molarities or molalities. For example, the equivalent fraction of M^{Z+} ($\overline{\mathrm{E_M}}$) in the sorbent can be calculated from

$$\overline{\mathrm{E_M}} = \frac{Z_{\mathrm{M}} q_{\mathrm{M}}}{\mathrm{Q}} \quad (9)$$

q_M is the ion concentration of M in solid phase (mmol/g) at equilibrium.

For elution studies of sorbent, the elution-% and the distribution coefficient at elution ($K_{\mathrm{d,elut.}}$) can be obtained from

$$Elution - \% = \left(1 - \frac{q_{eq}}{q_i}\right) \times 100 = \left\{1 - \frac{q_i - C_{eq}(V/m)}{q_i}\right\} \quad (10)$$

$$K_{d,elut.} = \frac{q_{eq}}{C_{eq}} = \left\{\frac{q_i - C_{eq}(V/m)}{C_{eq}}\right\} \quad (11)$$

Here q_i is the initial amount of M loaded in the solid phase, q_{eq} is the amount of M in solid phase after stripping, and C_{eq} is the equilibrium concentration of M in the stripping solution.

3 Experimental

3.1 Chemicals and regents

Three ion exchangers were synthesized for this work, namely α-ZrP, am-ZrP, and PAN-encapsulated am-ZrP. The chemicals $ZrOCl_2 \cdot 8H_2O$ and $ZrCl_4$ were the Zr sources of α-ZrP and am-ZrP materials, respectively. The chemicals $NaH_2PO_4 \cdot H_2O$ and H_3PO_4 were used as the P source for α-ZrP and am-ZrP materials, respectively. The polymer carrier PAN was used to encapsulate am-ZrP to form the porous beads. The metal salts $Co(NO_3)_2 \cdot 6H_2O$, $N_3NdO_9 \cdot 6H_2O$ and $DyN_3O_9 \cdot xH_2O$ were used to prepare the Co-Nd-Dy ternary equimolar solution and simulated leachate. The reagents HNO_3, H_2SO_4, H_3PO_4, or HCl were employed to study the batch elution and column elution studies.

3.2 Synthesis

3.2.1 Preparation of α-ZrP

α-ZrP was synthesized using a modified recipe from Rajeh and Sziertes [102]. Solutions of $NaH_2PO_4 \cdot H_2O$ (828.18 g) in 3 M HCl 600 (mL) and 322.25 g of $ZrOCl_2 \cdot 8H_2O$ in 300 mL deionized water were mixed in a 3-L glass Huber reactor (100 rpm). The obtained white homogeneous mixture was then allowed to stand for 24 h at 80°C and for another 24 h in room temperature. Subsequently, 3 L of 2 M HCl and 2 L of 2 M H_3PO_4 were sequentially used to wash the precipitate to remove unbound Na^+ and Cl^- ions. After washed with deionized water to pH 3, the product was dried in an oven at 65°C for 48 h. The dried white product was pretreated using 0.1M HNO_3 (solid:liquid ratio 1:10) by a rotating mixer at 23°C for 24 h. The α-ZrP was then rinsed with deionized water to approximately pH 3 and dried in an oven at 65°C for 48 h. The preconditioned product was ground and sieved to desired grain size (200-100 mesh) for further study.

Figure 4. Huber reactor (3 L) equipped with water bath used for preparation of α-ZrP

3.2.2 Preparation of am-ZrP

A precipitation method was used for am-ZrP material synthesis according to a previous report [103]. $ZrCl_4$ (30.7 g) was dissolved in HCl (430 mL, 2 M) and mixed with 400 mL of H_3PO_4 solution (1.25 M). The precipitate obtained was allowed to stand overnight. Subsequently, the white product was washed utilizing deionized water to pH 3. Then the am-ZrP was placed to oven and dried at 60^{o}C for 48 h. Finally the product was ground and sieved to desired grain size (200-100 mesh) for further study.

3.2.3 Preparation of am-ZrP/PAN

The am-ZrP/PAN composite was prepared using methods described previously [99, 100]. Solution A was prepared by mixing am-ZrP (7.2 g), DMF (84 mL), and Tween 80 (2 mL) for 2 h with magnetic stirring at 60°C. PAN (4.8 g) was added to solution A and continued stirring for another 2 h. The composite beads were made by a gelation process where the synthesis mixture was dropwise added to deionized water (2L) using a syringe pump and needle (0.6 mm). The formed beads were aged in deionized water for 24 h. The product was then rinsed with deionized water (2 L). The obtained product was dried by freeze-drying (Christ alpha 1-4 LSC) under 0.570 mbar at -26^{o}C.

3.3 Analytical methods

The structural study for materials used the characterization methods of X-ray powder diffraction (XRD), the characteristic Fourier transform infrared (FT-IR) spectra, thermogravimetry (TG) and solid-state ^{31}P magic angle spinning nuclear magnetic resonance (^{31}P MAS NMR) spectra.

For the morphology and spatial distribution study, scanning electron microscopy (SEM) and X-ray tomography were used.

An Agilent 4200 microwave plasma-atomic emission spectrometer (MP-AES) was used to determine the metal concentrations.

3.4 Experimental plan

α-ZrP, am-ZrP, and am-ZrP/PAN were developed for separation of the main components of an NdFeB magnet (Co, Nd and Dy) after a selective leaching procedure.

Due to the layered structure and reported high capacity (6.64 meq/g), α-ZrP was chosen as the first ion exchanger to make full use of the ion exchange site's inner and outside layers. We hoped that the layered structure of α-ZrP would bring additional selectivity due to the ion-sieve function of the interlayer spaces. A detailed research experimental design of paper I is presented in Figure 5.

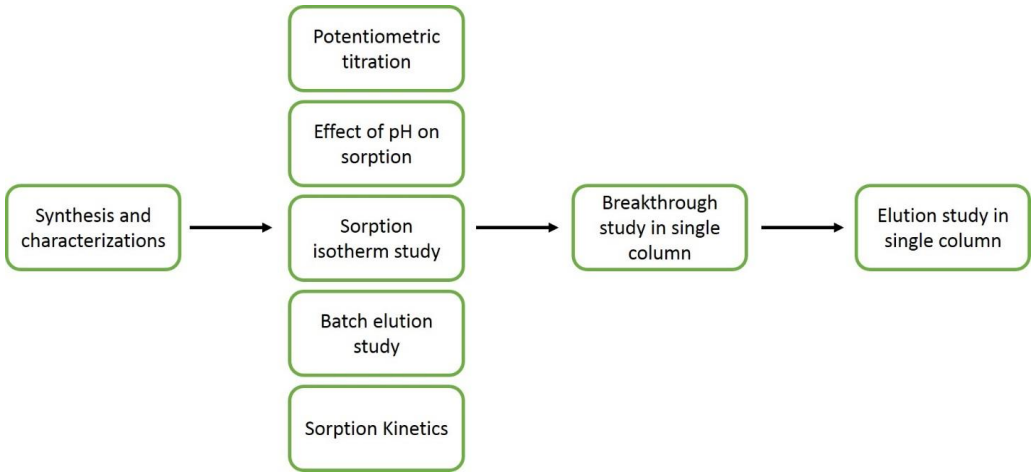

Figure 5. Flowchart of the research design content of Paper I

When compared with α-ZrP, am-ZrP has a larger specific surface area and contains numerous microspores and mesopores [104-106]. The experimental design flowchart of paper II is shown in Figure 6.

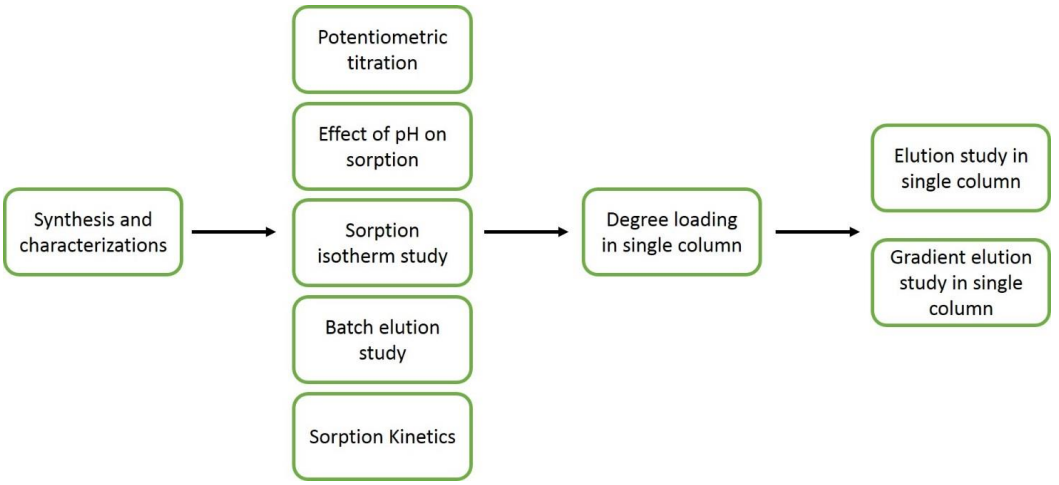

Figure 6. Flowchart of the research design content of paper II

When comparing the ion exchange results between α-ZrP and am-ZrP, am-ZrP showed better ion-exchange behaviour. In addition, column separation for Co, Nd, and Dy were achieved using single-column separation. These promising results led us to apply am-ZrP for the scale-up study for industry.

Am-ZrP in powdery form can easily cause operational problems, such as clogging in the pilot column operations. Thus, am-ZrP was difficult to apply in the pilot-scale test. To overcome this limitation, we employed PAN as the polymer carrier to encapsulate the am-ZrP into composite beads. Moreover, a gradient elution process was utilized for the purpose to achieve well separation. The column experiments were optimized by changing the feed concentration, running speed, operational temperature, and concentration of eluting agent (Figure 7).

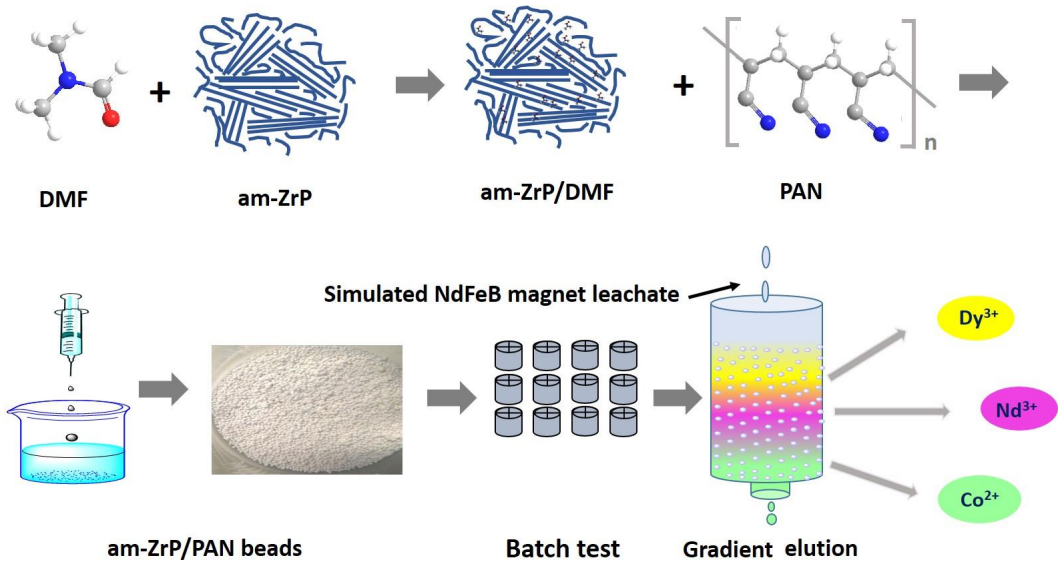

Figure 7. Experimental plan for paper III.

4 Results and discussion

4.1 Characterization of synthesis samples

4.1.1 Analysis and structure comparison between α-ZrP and am-ZrP

The synthesized α-ZrP is a platelet-like highly crystalline material with an interlayer space of 7.6 Å calculated from the (002) diffraction peak (Figure 8a). The SEM image shows regular crystals (Figure. 8b). In contrast, the synthesized am-ZrP had weak and broad X-ray diffraction (Figures 8d and 8e). The SEM image showed the amorphous nature of am-ZrP.

For the FT-IR spectrum, the feature band(s) of deformation and vibration of P-OH were observed at 1249, 1069, 1038, and 963 cm^{-1} for α-ZrP (Figure 8c) and 987 cm^{-1} for am-ZrP (Figure 8f).

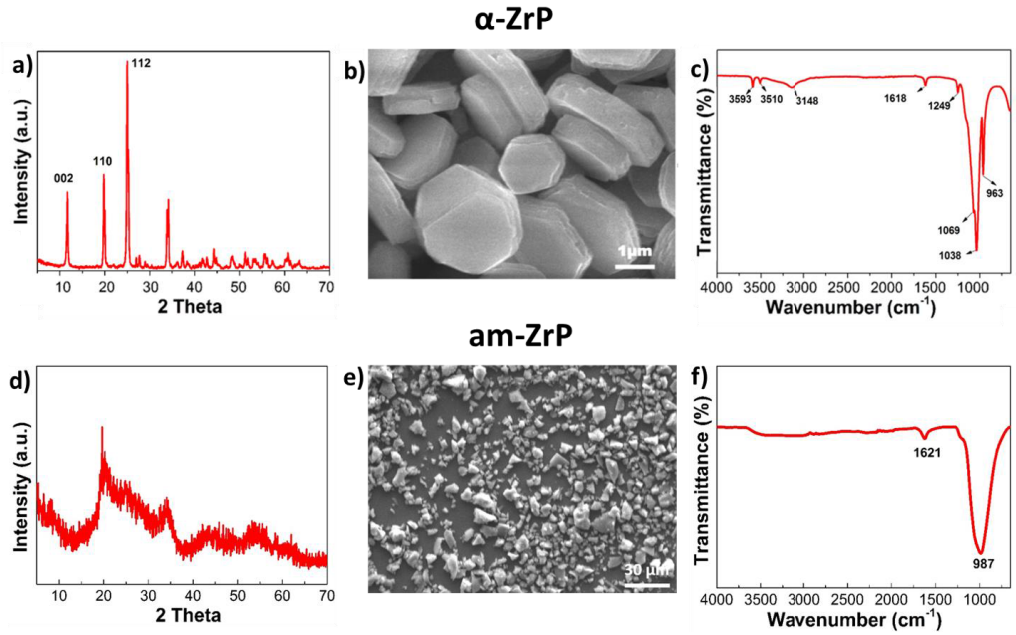

Figure 8. Characterization of synthesized α-ZrP. a) XRD pattern, b) SEM image, c) FT-IR spectrum. Characterization of synthesized am-ZrP. d) XRD pattern, e) SEM image, f) FT-IR spectrum.

α-ZrP was synthesized without hydrofluoric acid (HF). This was beneficial for production of the large crystal size of α-ZrP (diameter 1-4 μm) in this work synthesis (Table 4). The reaction was completed at lower temperature compared with the previous methods shown in Table 4. Am-ZrP was synthesized using an easily available method by precipitation at room temperature. Both syntheses were in agreement with the aims of green chemistry and were promising for pilot-scale application.

Table 4. Different methods for crystalline α-ZrP preparation

Synthesis method	Zr source	P Precursor	Temperature	Reaction time	Average diameter	Reference
Hydrothermal method	$ZrOCl_2 \cdot 8H_2O$	3 M H_3PO_4	200°C	24 h	~400 nm	[79]
	$ZrOCl_2 \cdot 8H_2O$	12 M H_3PO_4	200°C	24 h	1 μm	[79]
	$ZrOCl_2 \cdot 8H_2O$	3 M H_3PO_4, 5 M HF	100°C	24 h	1-4 μm	[79]
Refluxing method	$ZrOCl_2 \cdot 8H_2O$	3 M H_3PO_4	100°C	24 h	~60 nm	[79]
	$ZrOCl_2 \cdot 8H_2O$	12 M H_3PO_4	100°C	24 h	~200 nm	[79]
	$ZrOCl_2 \cdot 8H_2O$	6 M H_3PO_4	94°C	48 h	~120 nm	[107]
	$ZrOCl_2 \cdot 8H_2O$	10 M H_3PO_4	-	-	250 nm	[81]
	$ZrOCl_2 \cdot 8H_2O$	$NaH_2PO_4 \cdot H_2O$, 3 M HCl	80°C	24 h	1-4 μm	Paper I

4.1.2 Determination of molecular formula of am-ZrP

The composition of am-ZrP could be easily changed by adjusting the synthesis conditions. The elemental content was obtained from am-ZrP digestion experiments. The P/Zr ratio was determined to be 2.03. The three peaks of ^{31}P MAS NMR spectrum represented the three different phosphate groups, namely $-H_2PO_4$ (-13.6 ppm), $-HPO_4$ (-21.7 ppm), and $-PO_4$ (-27.5 ppm) (Figure 9a) [108, 109]. From the peak deconvolution, the ratio of these phosphate groups was estimated to be 9.3:100:4.8.

Two weight-loss steps were observed in the TG curve (Figure 9b). The release of physically bound water was suggested for the first weight loss step (7.07%; 25°C─184 °C) and the condensation of $-H_2PO_4$ was suggested for the second weight loss step (4.98%, 184°C─800°C) [110]. From the XRD pattern of the am-ZrP calcined at 800°C (Figure 9c), the substance was identified as ZrP_2O_7 [111], which was consistent with the P/Zr ratio of 2.03 from the digestion analysis.

Finally, after combining the results of the digestion experiment, ^{31}P MAS NMR spectrum, and TG analysis, the chemical formula of am-ZrP was determined to be $Zr(H_2PO_4)_{0.17}(HPO_4)_{1.78}(PO_4)_{0.09} \cdot 0.96H_2O$. Based on the calculated formulae, theoretical ion-exchange capacity of am-ZrP should be 6.97 meq/g.

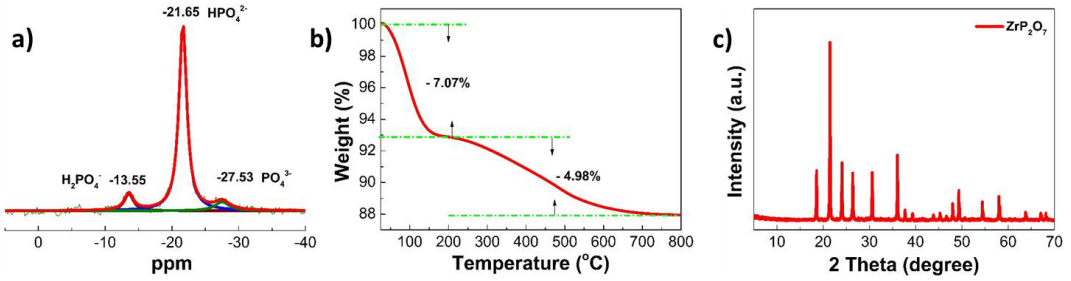

Figure 9. Characterization of synthesized am-ZrP. a) The deconvolution peaks based on ^{31}P MAS NMR spectrum, b) TGA curve, c) XRD pattern of am-ZrP calcined at 800°C.

4.1.3 Characterizations of synthesized am-ZrP/PAN composite

The regular am-ZrP/PAN spheres are shown in Figure 10a. Their size distribution was evaluated by analyzing a total of 199 particles in the perspective of volume and number distribution. The average bead size was 2 mm in diameter according to the data of equivalent (CE) measurements (Table 5). The circularity value was determined to range from 0.74 to 0.98 (Table 5), indicating a more or less spherical shape. A cross-section of the beads is shown in Figure 10b, which presents the imaged internal porous structure. This is the desired feature for the sorption material (Figure 10c) [94].

X-ray tomography demonstrated the porous feature of the beads and the more or less homogeneous distribution of the inorganic am-ZrP in the polymer matrix (Figure 10d). The porosity ratio of am-ZrP/PAN was determined to be approximately 40%. In addition, the spatial distribution of am-ZrP was characterized along the Z-axis of the bead with XY planes (blue arrow, Figure 10e). The spatial distribution study revealed that am-ZrP was quite evenly distributed in the inner surface and that there was slightly more am-ZrP near the bead surface than elsewhere.

Table 5. Analyzed particle parameters of am-ZrP/PAN beads

Name	Volume distribution			Number distribution		
	Minimum	Maximum	D [4, 3][a]	Minimum	Maximum	Mean
CE Diameter (μm)	1640	2341	2035	1640	2341	2010
Circularity	0.74	0.98	-	-	-	-

[a]D [4, 3] is the equivalent volume mean diameter

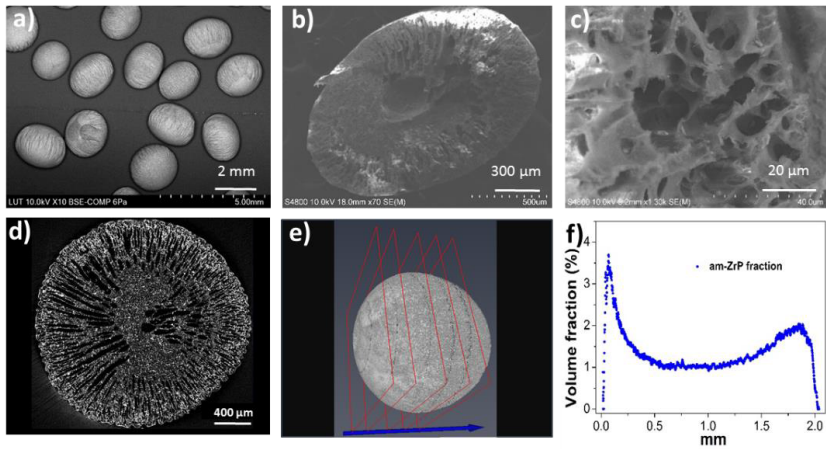

Figure 10. Synthesized am-ZrP/PAN beads. a) SEM image, b) SEM image of a bead's cross-section, c) SEM image for the porous structure, d) X-ray tomography image, e) spatial distribution as determined along the blue arrow (Z-axis of the bead) with XY-planes, f) curve of am-ZrP fraction (Z-axis direction).

The XRD pattern of am-ZrP shows a typical feature for amorphous ZrP. As am-ZrP (or semicrystalline ZrP) includes considerably small particles with a layered structure, the layered feature was revealed by weak and broad peaks [78, 80, 81]. The peak shifts were observed from 10.0° to 8.1° (2theta), indicating that the interlayer space was expanded from 9 to 10.8 Å (Figure 11). This phenomenon suggested that DMF was intercalated into the interlayer space. In previous studies, α-ZrP and α-SnP have been studied as the host for DMF intercalation [75, 112]. Double DMF molecules were suggested to be intercalated non-vertically to the interlayer with the hydrogen bond (P)-O-H···O-CH-(N), owing to the limited interlayer space (Table 6).

Table 6. DMF intercalation on α-ZrP/DMF, α-SnP/DMF, and am-ZrP/DMF

Inorganic material	Basal spacing (Å)	Intercalated basal spacing (Å)	Diameter of DMF (Å)	Reference
α-SnP	7.8	13.3	3.5	[75]
α-ZrP	7.6	11.2	3.5	[112]
am-ZrP	9.0[a]	10.8	3.5	this work

[a]Semicrystalline am-ZrP material.

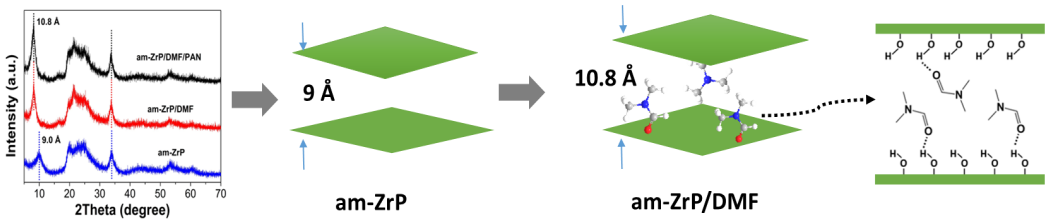

Figure 11. Illustration of the intercalation of DMF in semicrystalline ZrP based on XRD patterns.

The bands of the FTIR spectrum of the am-ZrP/PAN composite were consistent with the bands of the PAN beads and am-ZrP (Figure 12a). The strongest bands at 954 cm^{-1} and 1047 cm^{-1} are the P-OH deformation and the vibration of the orthophosphate group [113].

For the TG curves of am-ZrP/PAN beads, the elimination of free water molecules contributes to 8% mass loss (<300ºC) (Figure 12b). It was suggested that condensation of H_2PO_4 functional groups of am-ZrP and decomposition of PAN occurs from 300ºC to 700ºC [87]. The 56.7% am-ZrP content in the am-ZrP/PAN composite could be calculated based on the thermal analysis data from powdery am-ZrP, PAN beads, and am-ZrP/PAN beads.

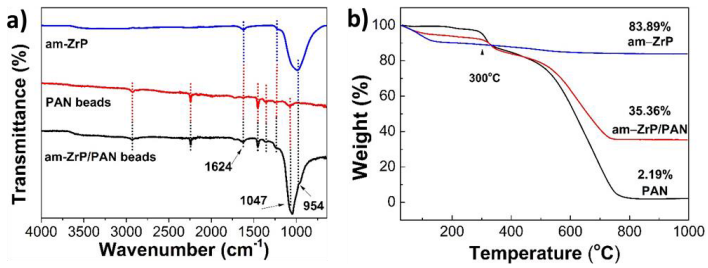

Figure 12. PAN beads, powdery am-ZrP, and am-ZrP/PAN beads. a) FTIR spectra, b) TGA curves.

4.2 Ion-exchange behaviour study

4.2.1 Potentiometric titration

The P-OH group in α-ZrP can be considered as a weak acid, which undergoes a dissociation reaction:

$$\text{P-OH} \leftrightarrow \text{P-O} + \text{H}^+ \qquad (12)$$

The acid dissociation constant K_a is defined as:

$$K_a = \frac{[PO^-][H^+]}{[POH]} \qquad (13)$$

Here, [POH] is the undissociated phosphate content (mM/g) of the material. $[PO^-]$ and $[H^+]$ are the concentrations of the dissociated phosphate and hydronium ion inside the pores of α-ZrP.

The degree of dissociation (β) of P-OH can be expressed as

$$\beta = \frac{[PO^-]}{[POH]+[PO^-]} \qquad (14)$$

After combining equations 13 and 14, the following equation is obtained:

$$log\frac{1-\beta}{\beta} = pK_a - p\text{H} \qquad (15)$$

β can then be calculated from the equation below:

$$\beta = \frac{1}{1+\frac{H^+}{K}} = \frac{1}{1+10^{pK_a-p\text{H}}} \qquad (16)$$

Typically, a 1.0 M $NaNO_3$ solution was used to keep a constant ionic strength. The initial exchange with $NaNO_3$ is inevitable.

$$\text{POH} + \text{Na}^+ \leftrightarrow \text{PONa} + \text{H}^+ \qquad (17)$$

As a result, the amount of the conversion to the Na form (q_{Na1}, mmol/g) from $NaNO_3$ can be obtained from the following:

$$q_{Na1} = ([H^+]_{eq} - [H^+]_i)\,(V/m) \qquad (18)$$

Here, $[H^+]_{eq}$ is the concentration of H^+ in the solution at equilibrium (mmol/L) and $[H^+]_i$ is the initial concentration of H^+ in the solution (mmol/L). V is the solution volume (mL) and m is the material mass (mg).

NaOH is subsequently used for titration. The reaction is described below as:

$$POH + NaOH \quad \leftrightarrow \quad PONa + H_2O \qquad (19)$$

The amount of the conversion to the Na form (q_{Na2}, mmol/g) from NaOH can be acquired from the equation:

$$q_{Na2} = ([OH^-]_i - [OH^-]_{eq})(V/m) \qquad (20)$$

where $[OH^-]_i$ and $[OH^-]_{eq}$ is the initial and the equilibrated solution concentrations, respectively.

The total ion exchange capacity (Q) of α-ZrP can be calculated from the summation of q_{Na1} and q_{Na2}:

$$Q = q_{Na1} + q_{Na2} = ([H^+]_{eq} - [H^+]_i + [OH^-]_i - [OH^-]_{eq})(V/m) \qquad (21)$$

The degree of crystallinity highly affects the titration behaviour. Amorphous materials often show a steady increase in titration curves. Normally, clear inflection points can be observed when titrating a material with high crystallinity [67, 76]. A total ion-exchange capacity of 6.6 meq/g has been obtained by NaOH titration of α-ZrP. The crystalline α-ZrP has been identified as a diprotic weakly acidic cation exchanger [68, 69].

In this work, ZrP displayed a diprotic character in titration curves (Figure 13). The ion-exchange capacity of a total of 6.6 meq/g was obtained with the first and second equivalence point at 5 meq/g and at 6.6 meq/g, respectively (Figure 14). To evaluate the pK_{a1} and pK_{a2} for the diprotic character of titration curves, the more acidic sites with the ion-exchange capacity of 5.0 meq/g (Q_1) and the weaker acidic sites of 1.65 meq/g (Q_2) were distinguished according to the apparent equivalence points in Figure 13. The pK_a-value was chosen from the middle point value of the plateaus of the titration curve, in this case the $pKa_1 = 3.5$ and $pKa_2 = 6.5$ were obtained.

The degree of dissociation for the more acidic sites and the weaker acidic sites can be calculated using the titration data from Eq. 16 and the equation below.

$$q_{Na} = \beta_1 Q_1 + \beta_2 Q_2 \qquad (21)$$

The best fit between Eq. 21 and 22 was then acquired when using p$Ka_{1'}$ (3.3) and p$Ka_{2'}$ (6.3). The $pK_{a1'}$ and $pK_{a2'}$ values are very close to the value we obtained from the titration curve.

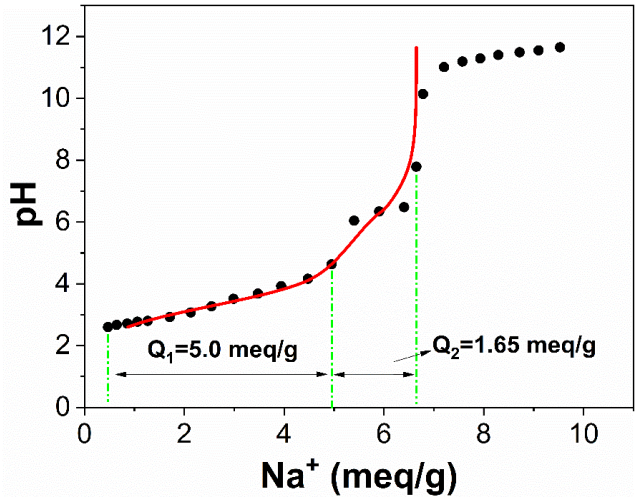

Figure 13. Titration curve of α-ZrP with 1.0 M NaOH in a 1.0 M $NaNO_3$ background.

The titration of am-ZrP was performed using a 1.0 M NaOH solution with 1.0 M $NaNO_3$ solution as background. The pH of the solution changed from an initial pH 6.5 (1.0 M $NaNO_3$) to pH 2.6 during equilibrium time, indicating a 2.13 meq/g conversion to the Na form (q_{Na1}). Adding this conversion value to the titration data, we observed that the ion-exchange capacity was 9.23 meq/g ($q_{Na1} + q_{Na2}$) as estimated from the inflection point of the plateau (Figure 14). This ion-exchange capacity value is higher than 6.97 meq/g as calculated from the chemical formula. This deviation might be due to the hydrolysis of material in alkaline solutions [110].

As for the individual pK_a values in crystalline α-ZrP, we have demonstrated how to determine its values from the titration curve and the relevant equations. These studies were only based on the apparent equivalence points in the titration curves. It was not possible to acquire these pK_a values from the steadily increasing titration curve of am-ZrP.

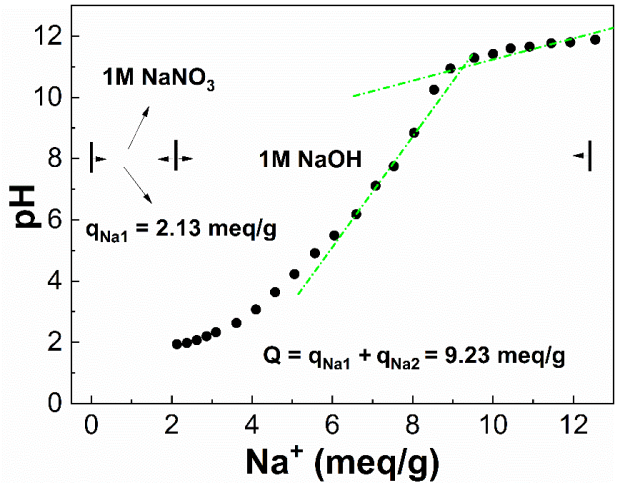

Figure 14. Titration curves of am-ZrP using 1.0 M NaOH in a background of 1.0 M $NaNO_3$ solution.

The titration of the PAN beads and am-ZrP/PAN beads was studied using 1.0 M $NaNO_3$ solution as background. The R-OH conversion to Na-form (q_{Na1}) can be calculated from the difference of the initial and equilibrium pH of the 0.1 M $NaNO_3$ solution (Eq. 20).

The q_{Na1} of the pure PAN beads was calculated to be 0.004 meq/g. This value was disregarded from further calculations because it was negligible. The total ion-exchange capacity of pure PAN beads was estimated 0.46 meq/g from the plateau of the titration curve (Figure 15a) [114]. The q_{Na1} for the am-ZrP/PAN beads was calculated to be 0.53 meq/g. The total ion-exchange capacity (q_{Na1}+q_{Na2}) of am-ZrP/PAN beads was estimated 4.5 meq/g. (Figure 15b).

The am-ZrP content in the beads was calculated to be 56.7% based from the TG analysis. In addition, the am-ZrP content of am-ZrP/PAN beads can be estimated based on the theoretical capacity (6.97 meq/g) of am-ZrP and the capacity (4.5 meq/g) of am-ZrP/PAN beads. Using the ion-exchange capacities of the am-ZrP/PAN composite, the am-ZrP content in the beads was calculated to be 57.9%, which is consistent with the value from the TG analysis.

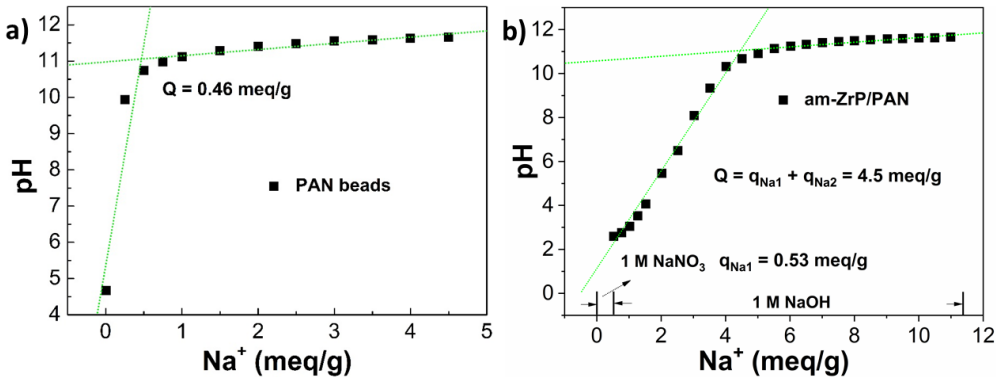

Figure 15. Titration curves of the PAN beads a) and the am-ZrP/PAN beads b) in 1.0 M $NaNO_3$.

4.2.2 Effect of pH on sorption

The effect of pH on metal sorption of α-ZrP, am-ZrP, and am-ZrP/PAN was investigated using 1.0 mM equimolar Co, Nd, and Dy nitrate solution. The uptake amounts for these ion exchangers are shown in Table 7. α-ZrP and am-ZrP showed a similar total metal uptake of 1.6 meq/g at equilibration pH ~3.5. However, am-ZrP had a higher separation factor (SF) based on the K_d value in Figure 16 a, b and c. The SFs of am-ZrP were calculated to be 6.5, 2.1, and 3.2, corresponding to pH 1.0, 1.8, and 2.6, respectively (Figure 16b). Dy was found to be the most favoured element obtained for am-ZrP materials based on the values of K_d(Co)=6 mL/g, K_d(Nd)=180 mL/g, and K_d(Dy)=458 mL/g at pH 1.8. In addition, compared with the total uptake amount, the equivalent-% of Co was not more than 3% at pH below 3, indicating excellent potential separation of Co from Nd and Dy. For am-ZrP/PAN, the strong sorption of Co after pH 4 caused the obviously decrease of the Nd and Dy K_d values (Figure 16c).

For the uptake amount of am-ZrP/PAN, we observed that the metal uptake by am-ZrP increased approximately 50% at pH 3.5 (Table 7) when focused only on the inorganic counterpart. The value was calculated to be 2.43 meq/g for am-ZrP in am-ZrP/PAN beads compared to 1.65 meq/g of pristine am-ZrP. This phenomenon was suggested to result from the DMF intercalation to the layers of ZrP. It is reported that the rather large hydrated metal ions such as REEs are inaccessible in the cavity of the layer due to diffusional resistance [115]. However, with the interlayer space expansion from 9 Å to 10.8 Å after DMF intercalation, the ion-exchange sites became accessible for the hydrated metal ions. Therefore, sorption efficiency was improved and the metal uptake amount increased.

Table 7. Metal uptake data on α-ZrP, am-ZrP, and am-ZrP/PAN in the initial concentration as 1.0 mM equimolar Co, Nd, and Dy.

Material	pH_{eq}	Co (meq/g)	Dy (meq/g)	Nd (meq/g)
α-ZrP	3.5	0.44	0.61	0.63
am-ZrP	3.4	0.43	0.62	0.61
am-ZrP/PAN	3.5	0.26	0.58	0.59

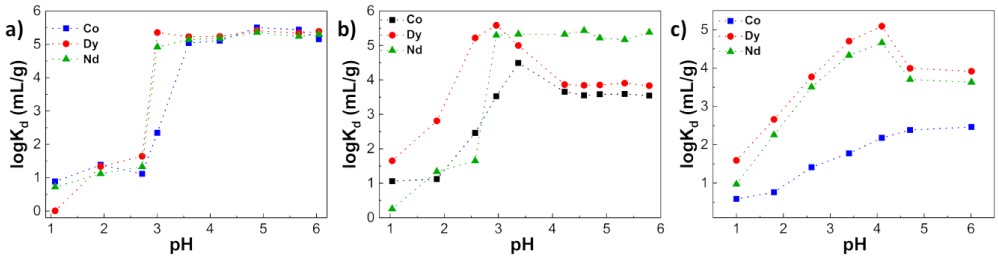

Figure 16. Distribution coefficients of the metal sorption of 1.0 mM equimolar Co, Nd, and Dy nitrate solution. a) α-ZrP, b) am-ZrP, c) am-ZrP/PAN.

When increasing the metal concentration to 2.0 mM, there is no obvious plateau shown in the uptake curves of α-ZrP (Figure 17a). However, the two separate K_d linear figures were based on the two acid-exchange sites of α-ZrP at pH 1 to 5.3 and pH 5.3 to 6.4 (Figure 17b and 17c). The log K_d versus pH showed a low slope (0.33-0.59) in the first domain and a considerably larger slope (2.25-2.42) in the second domain. This phenomenon indicates that the less acidic exchange site (pK_{a2}=6.3) was used for exchanging with the REE and Co ions.

Visual Minteq Software was used to calculate the solubility of Co, Nd, and Dy at the ranges of pH and the metal concentrations [116]. There was no indication of precipitation throughout the study.

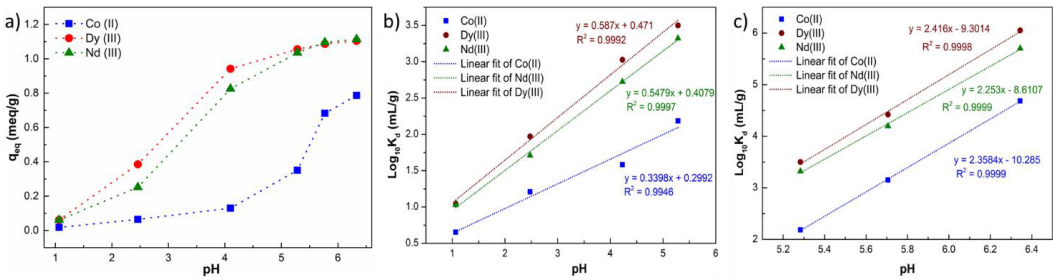

Figure 17. a) Effects of equilibrium pH on the metal sorption of 2.0 mM equimolar Co, Nd, and Dy nitrate solution. Distribution coefficients on the metal sorption by α-ZrP from a 2.0 mM equimolar Co, Nd, and Dy nitrate solution at equilibrium pH. b) Linear fitting of log K_d over pH 1.0 to 5.3. c) Linear fitting of log K_d over pH 5.3 to 6.3.

4.2.3 Sorption isotherm study

The sorption isotherms of α-ZrP were investigated at approximately pH 2.5 and pH 4.5 at equilibrium state. The metal uptakes of Nd and Dy showed an increasing trend following the equilibrium concentration of the metal, increasing until a plateau emerged approximately at 3.2 mM to 3.6 mM at pH 2.5 (Figure 18a). In contrast, the uptake of Co decreased after the equilibrium concentration of 3 mM. As Nd and Dy have higher affinity than Co, Co was replaced by Dy and Nd as the concentration of Nd and Dy increased. At pH 4.5, we observed that Co and Nd uptake started to decrease after the equilibrium concentration at approximately 2.0 mM (Figure 18b). Therefore, the order of preference for metal adsorption by α-ZrP is Dy>Nd>Co.

Compared to α-ZrP, higher metals uptake was found by am-ZrP at $C_{in.}$ 5.0 mM and pH 2.5 (Figure 18c). The total metals uptake of am-ZrP (3.4 meq/g) was approximately five times larger than that of α-ZrP (0.6 meq/g) (Table 8). In addition, α-ZrP and am-ZrP showed the same order of preference Dy>Nd>Co, also Co uptake was rather low on α-ZrP and am-ZrP at pH 2.5 or pH 4.5 (Table 8).

Table 8. Analyzed data for the sorption isothermal study of α-ZrP and am-ZrP

Ion exchanger	$pH_{eq.}$ (equilibrium)	$C_{in.}$ (initial concentration)	Uptake (meq/g)			Co (Equivalent-%)
			Co	Nd	Dy	
α-ZrP	2.5	5.0 mM	0.02	0.18	0.40	3.3%
α-ZrP	4.5	5.0 mM	0.20	1.1	1.5	7.1%
am-ZrP	2.5	5.0 mM	0.18	1.5	1.7	5.3%

Equivalent-% is the percentage calculated from single metal uptake (meq/g) compared with the total metal uptake (meq/g).

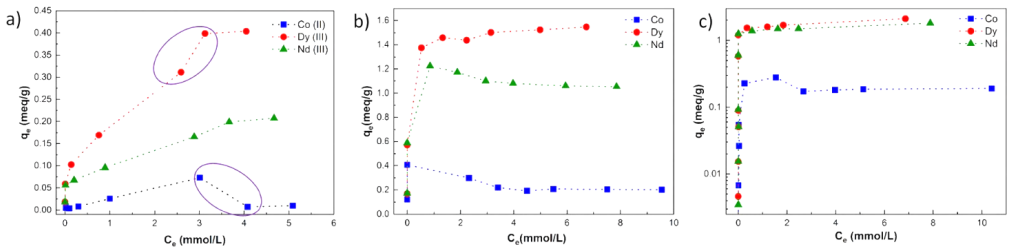

Figure 18. Isothermal sorption curves of Co, Nd, and Dy nitrate solution. a) α-ZrP at approximately pH_{eq} 2.5, b) α-ZrP at approximately pH_{eq} 4.5, c) am-ZrP at approximately pH_{eq} 2.5.

4.2.4 Batch elution study

To choose the right mineral acid for the column elution study, batch elution was necessary as pre-test experiments. For this work, four different acids at two concentrations were tested (Table 9). The most efficient total elution (96.7% Dy and 99.1% Nd) was obtained using 0.1 M H_2SO_4 as eluent for α-ZrP. Compared to other acids the difference in elution percentage was significant (>25%) and also a difference in eluent concentration was observed. An increase in H_2SO_4 concentration decreased the elution. That is unusual and was not seen with the other acids. SF (the ratio of K_d) was calculated based on the K_d values. HCl would be a good candidate due to a SF (Dy/Nd) of 3.08 at a concentration of 1.0 M (Table 9). However, HCl was not adopted in our work due to its high corrosiveness.

For am-ZrP, H_2SO_4 was also the most efficient when compared to the elution results of other acids. We observed that 85% Nd and 83% Dy were removed by 1.0 M H_2SO_4 (Table 9). The elution efficiencies of acids at 0.1 M was observed as H_2SO_4>HNO_3 >HCl >H_3PO_4. HCl and H_3PO_4 showed

less than 30% elution at this concentration. The separation factors calculated from K_d values of Dy and Nd show a decreased order as HCl (1.8)>HNO_3 (1.2)>H_2SO_4 (0.9)>H_3PO_4 (0.7).

Table 9. Batch elution data of α-ZrP and am-ZrP in different mineral acids

Stripping agent		α-ZrP					am-ZrP				
		Elution (%)		K_d (ml/g)		SF	Elution (%)		K_d (ml/g)		SF
(Mol/L)		Dy	Nd	Dy	Nd	Dy/Nd	Dy	Nd	Dy	Nd	Dy/Nd
HCl	0.1	62	67	121	96	1.3	19	29	860	490	1.8
	1.0	92	97	17	5.6	3.1	78	73	56	75	0.8
HNO_3	0.1	70	65	85	105	0.8	57	60	153	132	1.2
	1.0	86	93	30	16	1.9	75	71	67	82	0.8
H_3PO_4	0.1	22	5.7	699	3239	0.2	12	8.6	1458	2102	0.7
	1.0	82	92	43	16	2.6	73	75	73	66	1.2
H_2SO_4	0.1	96	99	26	21	1.3	78	75	57	67	0.9
	1.0	85	89	35	24	1.5	85	83	35	42	0.8

4.2.5 Sorption kinetics

For the sorption kinetics study, a pseudo-first-order equation, pseudo-second-order equation, and simplified model of resistance to intraparticle diffusion were employed to determine the characteristic sorption constants of α-ZrP and am-ZrP [30-32].

The pseudo-first-order equation, the pseudo-second-order equation, and the intraparticle diffusion model were as follows:

$$\log(q_e - q_t) = \log q_e - \left(\frac{k_1}{2.303}\right)t \quad (25)$$

$$\frac{t}{q_t} = \frac{1}{k_2 q_e^{\,2}} + \frac{1}{q_e} t \qquad (26)$$

$$q_t = k_{\text{int}} t^{1/2} + C \qquad (27)$$

Here q_e is the maximum uptake value at equilibrium and q_t is the uptake value at any time t. The rate constants k_1 and k_2 belong to the pseudo-first-order and the pseudo-second-order models, respectively. The slope k_{int} is the intraparticle diffusion constant. If a straight line can be obtained from a plot of q_t versus $t^{1/2}$, the adsorption mechanism should follow the process of intraparticle diffusion.

We observed that the metal uptake by α-ZrP increased with time, increasing until equilibrium was almost reached at 24 h (Figure 19a). A shorter time period of 12 h was observed in reaching equilibrium for the sorption by am-ZrP and am-ZrP (Figure 19b and 19c). At this point (12 h), the total uptake value for Dy and Nd were 1.27 meq/g (am-ZrP) and 1.37 meq/g (am-ZrP/PAN), respectively. All three ion-exchangers followed the pseudo-second-order model. The results suggest that the rate-limiting step for the adsorption of metal ions is the ion-exchange process [118-120].

For the am-ZrP/PAN composite, an intraparticle diffusion model based on Fick's law was used to determine the diffusion coefficients [117].

The intraparticle diffusion model based on Fick's law is as follows:

$$\begin{aligned} &\frac{\partial \hat{q}_j}{\partial t} = \frac{1}{r^2}\frac{\partial}{\partial r}\left(r^2 D_j \frac{\partial \hat{q}_j}{\partial r} \right), \\ &\left.\frac{\partial \hat{q}_j}{\partial r}\right|_{r=0} = 0, \quad \hat{q}_j\big|_{r=r_p} = f\left(c_j\right) \end{aligned} \qquad (28)$$

here D_j, $\hat{q}_j$, and r are the intraparticle diffusion coefficient, local concentration, and radial coordinate of species j, respectively.

Metal uptake by the am-ZrP/PAN composite was reasonably fast, even though the material's particle size was approximately 2 mm in diameter (Fig. 19d). The value of D_{Dy} $1.05 \cdot 10^{-13}$ m^2/s (R^2=0.937) and D_{Nd} $1.02 \cdot 10^{-13}$ m^2/s (R^2=0.967) were an order of magnitude lower than that of D_{Co} $4.31 \cdot 10^{-12}$ m^2/s (R^2=0.990), most likely due to their larger hydrated radii [121, 122].

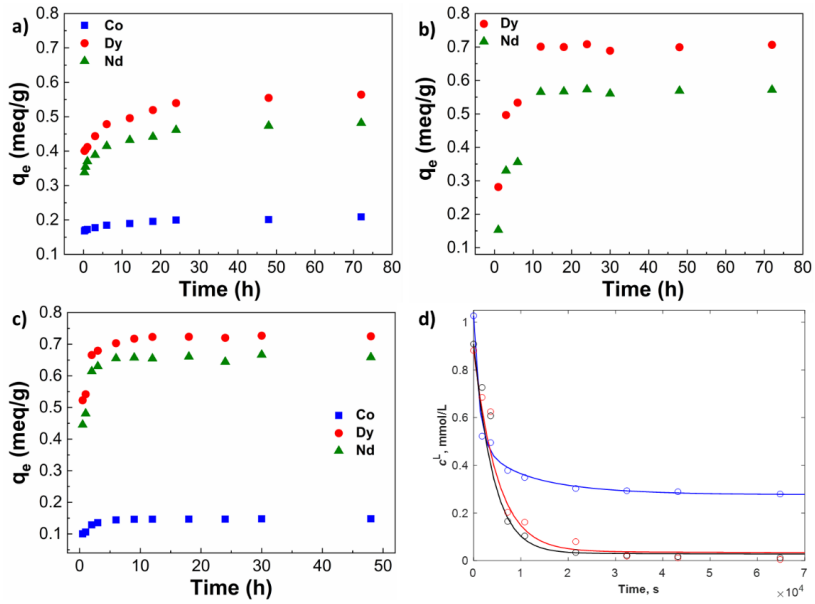

Figure 19. Kinetics curves of Co, Nd, and Dy adsorbed by a) α-ZrP, b) am-ZrP, and c) am-ZrP/PAN composite (23°C, pH 3). d) Simulation curves based on intraparticle diffusion model according to the kinetics curves of the am-ZrP/PAN composite.

4.3 Column experiments

4.3.1 Loading and breakthrough

The metal loading on columns of α-ZrP, am-ZrP, and am-ZrP/PAN materials were tested using 1.0 mM equimolar Co, Nd, and Dy.

The breakthrough of Co was observed first and followed by Nd and Dy (Figure 20a, b and c). This suggests that the metals were preferred by these ion-exchange materials in the order Dy>Nd>Co. The loaded amount of Co relative to the total metal loading amount ranged from 0.8 to 3.7 equivalent-% (Table 10). When compared with α-ZrP, am-ZrP displayed a higher total metal loading capacity (2.4 meq/g), less Co, and a larger equivalent Dy/Nd ratio (1.9).

The column (am-ZrP) breakthrough points of Co, Nd, and Dy were observed at 20, 125, and 135 BV, respectively (Table 10, Fig. 20b). The Co desorption from loaded column was indirectly observed by

the Co concentration, which exceeded approximately 20% to that of the initial feed. Thereafter, a desorption of Nd also took place at 190 BV. This was caused by the exchange of Nd to Dy, since Dy has the strongest affinity on am-ZrP.

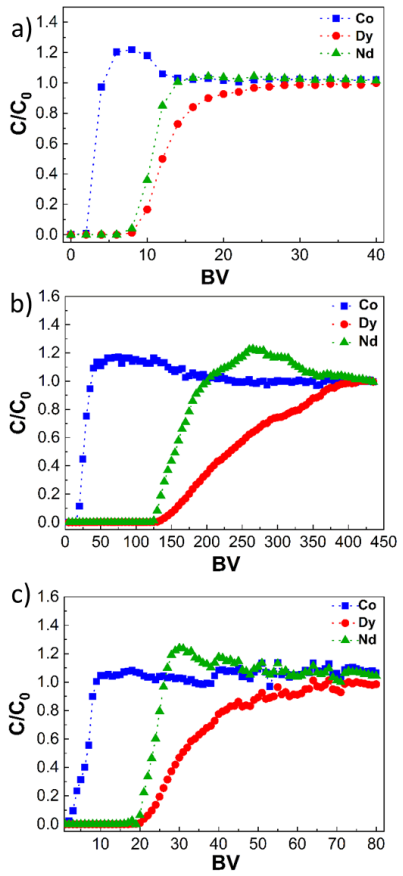

Figure 20. Breakthrough curves of Co, Nd, and Dy with initial concentrations of 1.0 mmol/L equimolar nitrate solution. a) α-ZrP at pH 2.5, b) am-ZrP at pH 1.8, c) am-ZrP/PAN at pH 1.8.

Even though the am-ZrP/PAN composite beads are of relatively large size (approximately 2 mm in diameter), the Co, Nd, and Dy loading equivalent percentages closely resembled these values of equivalent percentages when using the powdery am-ZrP as ion exchanger (Table 10). The higher concentration of Co between 8 to 20 BV and subsequently Dy after 20 BV was observed, indicating the same preferred order (Dy>Nd>Co) as pristine am-ZrP. Moreover, it is worth noting that the value of equivalent ratio (2.0) between the loaded amount of Dy and Nd was better than that of the powdery am-ZrP (1.9).

Table 10. Data of the column loading experiments under the loading solution of 1.0 mmol/L equimolar Co, Dy, and Nd

Materials	pH of feed	Breakthrough point (BV)			Loaded amount (meq/g)			Equivalent-%			Equivalent ratio (Dy/Nd)
		Co	Nd	Dy	Co	Nd	Dy	Co	Nd	Dy	
α-ZrP	2.5	2	8	8	0.01	0.07	0.11	3.7	37.2	59.1	1.6
Am-ZrP	1.8	20	125	135	0.02	0.83	1.57	0.8	34.4	64.8	1.9
Am-ZrP/PAN	1.8	2	20	22	0.03	0.38	0.78	2.5	31.9	65.6	2.0

Equivalent ratio is the ratio of metals uptake (meq/g).

4.3.2 Metal elution

We wanted to have single metal elution from the single-column study. For the α-ZrP packed column, HNO_3 at different concentrations and mixed with H_3PO_4 was tested for elution of loaded metals. With a fully loaded column it was not possible to have separate metal elution bands. To see clear elution bands of a single metal, the degree of metal loading must be considered.

To achieve better separation, a multistep gradient elution process was employed for the separation study by stepwise variation of the elution solution (HNO_3) concentration [123]. The am-ZrP material, with its more favourable ion-exchange properties, was employed to conduct the column separation for the Co, Nd, and Dy mixture. Decreasing the metal loading% to 8%, three separate elution bands were obtained with only a slight overlap from 25 to 32 BV (Figure 21a). The outlet order of metals (Co>Nd>Dy) was reversed with the adsorption order. Under these conditions, pure Co, Nd, and Dy can be produced (Figure 21a).

To set more realistic separation data, higher metal concentrations were tested using am-ZrP/PAN. A higher concentration solution totalling 1.2 g/L (approximately 10.7 wt% Co, 41.1 wt% Nd, and 48.2 wt% Dy) was used as the feed. Also the effect of higher temperature was tested. Thus, the gradient elution using 0.1, 0.2, 0.5 and 1 M HNO_3 at 50^{o}C was performed with the column loaded at approximately 10%. Compared with the initial concentration, the concentrations of Co, Nd, and Dy

in the outlet were significantly enhanced with the gradient elution and the possibility to enrich Co by this process is seen possible (Figure 21b).

Finally, a simulated magnet leachate was employed as feed to test the suitability of metal separation in a practical setting using the am-ZrP/PAN beads. A total metal concentration of 7.6 g/L (1.4 wt% Co, 9.3 wt% Dy, and 89.3 wt% Nd) was prepared based on previous reports [47, 124]. Although the gradient elution method was utilized to elute metals at 50ºC from an approximately 10%-loaded column (Figure 21c), the separation and recovery of Nd and Dy is extremely difficulty due to the high Nd concentration in the feed and the higher selectivity of Dy over Nd.

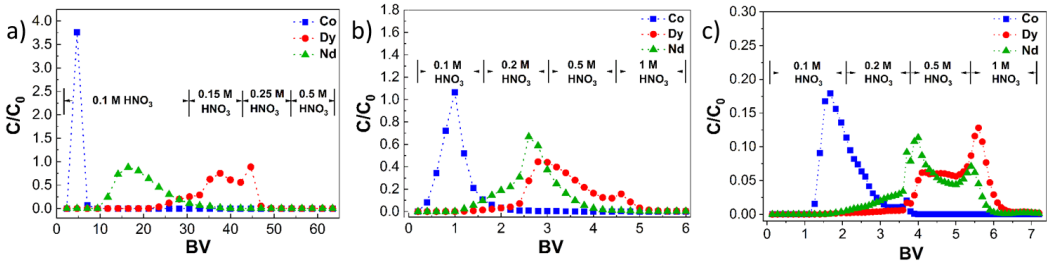

Figure 21. Gradient elution curves of Co, Nd, and Dy in the initial feed at pH 1.8 in 1 BV/h. a) The am-ZrP (approximately 8% degree loading) in feed at 1.0 mM at 23ºC. b) am-ZrP/PAN (approximately 10% degree loading) in 1.2 g/L feed at 50ºC. c) The am-ZrP/PAN (approximately 10% degree loading) in simulated magnet leachate (7.6 g/L) at 50ºC.

4.3.3 Stability of the material in regeneration

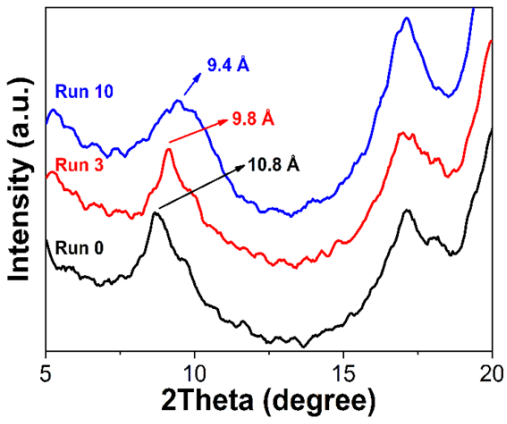

Figure 22. XRD pattern of fresh and used am-ZrP/PAN beads for Run 3 and Run 10 in the column.

In general, the α-ZrP and am-ZrP materials are stable in acidic solution as they are synthesized from strongly acidic precursors. The decrease of interlayer space 1.0 Å and 1.4 Å was observed from am-ZrP/PAN after Run 3 and Run 10 compared with the unused one (Figure 22). These results suggest that the intercalated DMF in the layers was gradually released during the column process. The XRD pattern displayed the layers was possible to gradually shrink in the using process.

5 Conclusions

In this work, α-ZrP ($Zr(HPO_4)_2 \cdot H_2O$) and am-ZrP ($Zr(H_2PO_4)_{0.17}(HPO_4)_{1.78}(PO_4)_{0.09} \cdot 0.96H_2O$) were synthesized and tested for the ability to recover and separate Co, Nd, and Dy metal ions. Crystalline α-ZrP showed a low sorption amount, which suggests that the exchanging metals cannot diffuse through the interlayer cavity in large extent. The sorption preference order Dy>Nd>>Co of α-ZrP and am-ZrP was obtained from batch ion-exchange experiments. We found that both materials had reasonable total metal capacity for Co, Nd, and Dy from equimolar solution but Co was not preferred. Am-ZrP had a higher selectivity and a higher sorption capacity when compared with that of α-ZrP or even the commercial classic Chelex 100 resin.

A gradient elution method proved to be an efficient process to achieve almost complete separation of metals using am-ZrP as ion-exchanger. Column loading at low degree has been shown to provide sufficient space for separate metal bands to develop in the elution process. Pure metal effluents were obtained by the gradient elution method using HNO_3 at different concentrations at room temperature. After obtaining promising results, larger lab-scale column separation was tested by using PAN-encapsulated am-ZrP composite in order to avoid possible operational problems associated with powdery am-ZrP.

X-ray tomography demonstrated a good spatial distribution of ion-exchange active component am-ZrP in the polymer matrix. Based on the batch experiments, the am-ZrP/PAN composite showed almost 50% higher sorption when compared to pristine am-ZrP. It appeared that the expansion of interlayer due to DMF intercalation enabled metals entering the cavity of the interlayer, resulting in increased uptake. This work demonstrated that it is possible to obtain fractions of Co with significantly improved purity relative to the simulated NdFeB magnet leachate through the single column form. However, it was not possible to achieve complete Nd and Dy separation due to the high Nd concentration in the simulated leachate solution and the higher Dy selectivity of the material.

Future work should consider the following two perspectives. From a material development perspective, enhanced uptake is suggested due to the intercalation of DMF. This provides a means for future study on intercalation chemistry and inorganic-organic hybrid materials.

From a process design perspective, even though it was difficult to achieve complete separation for the simulated leachate by single column, using multiple columns or a continuous simulated moving bed could be promising for future purification study.

Appendix

1 Methods for structural study

X-Ray Powder diffraction

X-Ray Powder diffraction (XRD) is primarily used for identification of crystalline material [125]. From these measurements, α-ZrPs can be identified by its unique diffraction peaks, such as (002), (110), and (112) plane. The interplanar spacing ($d_{h\,k\,l}$) can be calculated by Bragg's law (Equation 13).

$$\lambda = 2\, d_{h\,k\,l} \sin\theta \quad (1)$$

The XRD patterns were obtained by utilizing a Philips PW 3710 X-ray diffractometer operated with Cu-Kα (λ=1.542 Å) radiation (40 kV and 40 mA). The data were recorded from 5° to 70° in 2θ (step length 0.02°, counting time 0.5 s per step).

Fourier transform infrared spectra

Fourier transform infrared (FT-IR) spectra was used to identify the chemical group in the material by means of detecting the infrared absorption caused by certain bond vibrations [126].

Here, FT-IR spectra was employed to identify the POH group from the synthesized and relevant materials. FT-IR spectra were acquired using a Perkin Elmer spectrum one FT-IR spectrometer in ATR (attenuated total reflection) modle. The measurement range is from 600 to 4000 cm^{-1} at a resolution of 4.0 cm^{-1}.

Thermogravimetric analysis

Thermogravimetry (TG) is a technique to measure the changes in mass of a material against temperature changes in a specific atmosphere. The measurements are often simultaneously processing combined thermogravimetry and differential thermal analysis [127].

TG analysis was performed using a Mettler Toledo TG850. Samples were normally heated to 800°C or up to 1000°C when needed. The heating rate was programed as 5°C/min, as the measurement atmosphere depends on the measurement of program setting in nitrogen or air flow.

Solid-state ^{31}P magic angle spinning nuclear magnetic resonance

Solid-state ^{31}P magic angle spinning nuclear magnetic resonance (^{31}P MAS NMR) spectra were used for detecting phosphorous in different chemical environments. The different phosphate groups in am-ZrP can therefore be distinguished. The ratio of these phosphate groups can be obtained based on the

peak deconvolution results. The molecular formula can then be calculated from the combination of the ratio of these phosphate groups and the TG results.

^{31}P MAS NMR spectra were recorded from a Bruker Avance III NMR spectrometer (500 MHz, 4 mm H/X/Y MAS probe). The sample was placed into a zirconia rotor (4 mm). The sample of ^{31}P MAS NMR spectra recorded with a MAS rate (12 KHZ), 90° pulse (77 KHZ RF), and a 100-s recycle delay (64 scans).

2 Methods for morphology and spatial distribution study

Scanning electron microscopy

Scanning electron microscopy (SEM) was utilized to record the surface and the cross-section morphology of the synthesized samples.

The sample images were collected using a Hitachi Hi-Tech S-4800 field-emission scanning electron microscope (FESEM) by sputtering for deposition of a 3 nm-thick layer of Pd-Au.

For the size distribution investigation of the am-ZrP/PAN composite beads, samples without coating were imaged using a Hitachi SU3500 scanning electron microscope. In addition, Malvern Morphologi G3 software was employed to analyse the morphology of 199 beads from an SEM image.

X-ray tomography

X-ray tomography was used to reveal a structure's internal attributes by generated 3-dimensional imaged volumes from 2-dimensional X-ray image slices [128].

For spatial distribution of am-ZrP in an am-ZrP/PAN bead, the bead was recorded using a GE phoenix v|tome|x s 240. An optional nanofocus tube (180 kV/15 W, 90-kV, 300-μA) was used in a 27-W tube power. The sample was obtained with an isotropic 1.33-μm resolution/voxel size. 2700 projections (exposure time: 2 × 4000 ms) were performed using a 4000-ms skip at each angle for 9 h total.

3 Method for metals determination

Microwave plasma-atomic emission spectrometer

An Agilent 4200 microwave plasma-atomic emission spectrometer (MP-AES) was utilized to determine the metal concentrations. The OneNeb nebulizer and a double-pass cyclonic spray chamber was equipped for sample introduction.

The analytical cycle was a 30-s rinse with nitric acid (v/v 5%) and a subsequent 30-s sample uptake with pump speed 15 rpm. The internal standard and the buffer ion was used by adding 0.1 mL of La

(1000 mg/L) and 0.1 mL Cs (100 000 mg/L) into the 9.8 mL diluted samples. The detection wavelength of Co, La, Nd, and Dy was set at 340.512, 394.910, 430.358 and 353.171 nm, respectively.

Reference

1. Hu, B., et al., *Handbook of rare earth elements: analytics*. 2017: Walter de Gruyter GmbH & Co KG.
2. Kumari, A., et al., *Process development to recover rare earth metals from monazite mineral: a review.* Miner. Eng., 2015. **79**: p. 102-115.
3. Xie, F., et al., *A critical review on solvent extraction of rare earths from aqueous solutions.* Miner. Eng., 2014. **56**: p. 10-28.
4. Huang, C.-H., *Rare earth coordination chemistry: fundamentals and applications*. 2011: John Wiley & Sons.
5. Krishnamurthy, N. and C.K. Gupta, *Extractive metallurgy of rare earths*. 2004: CRC press.
6. Moeller, T. and H.E. Kremers, *The basicity characteristics of scandium, yttrium, and the rare earth elements.* Chem. Rev., 1945. **37**(1): p. 97-159.
7. Hatanaka, T., et al., *Rationally designed mineralization for selective recovery of the rare earth elements.* Nat. Commun., 2017. **8**: p. 1-10.
8. Jha, M.K., et al., *Review on hydrometallurgical recovery of rare earth metals.* Hydrometallurgy, 2016. **165**: p. 2-26.
9. Binnemans, K., et al., *Recycling of rare earths: a critical review.* J. Clean. Prod., 2013. **51**: p. 1-22.
10. European Commission, *Report on the critical raw materials for the EU*. 2017. p. 1-8.
11. Alonso, E., et al., *Evaluating rare earth element availability: A case with revolutionary demand from clean technologies.* Environ. Sci. Technol., 2012. **46**(6): p. 3406-3414.
12. Gutfleisch, O., et al., *Magnetic materials and devices for the 21st century: stronger, lighter, and more energy efficient.* Adv. Mater., 2011. **23**(7): p. 821-842.
13. Yang, Y., et al., *REE recovery from end-of-Life NdFeB permanent magnet scrap: A critical review.* J. Sustain. Metall., 2017. 3(1) p. 122-149.
14. Gutfleisch, O., et al., *Magnetic materials and devices for the 21st century: stronger, lighter, and more energy efficient.* Adv. Mater., 2011. **23**(7): p. 821-842.
15. Binnemans, K., et al., *Rare earths and the balance problem: how to deal with changing markets?* J. Sustain. Metall., 2018. **4**(1): p. 126-146.
16. Binnemans, K., et al., *Rare-earth economics: the balance problem.* Jom, 2013. **65**(7): p. 846-848.
17. Venkatesan, P., et al., *Selective electrochemical extraction of REEs from NdFeB magnet waste at room temperature.* Green Chem., 2018. 20: p. 1065-1073.
18. Binnemans, K. and P.T. Jones, *Rare earths and the balance problem.* J. Sustain. Metall., 2015. 1(1): p. 29-38.
19. Graedel, T.E., et al., *What do we know about metal recycling rates?* J. Ind. Ecol., 2011. **15**(3): p. 355-366.
20. Reck, B.K. and T. Graedel, *Challenges in metal recycling.* Science, 2012. **337**: p. 690-695.
21. El-Moneim, A., et al., *The influence of Co and Ga additions on the corrosion behavior of nanocrystalline NdFeB magnets.* Corrosion Sci., 2002. **44**(8): p. 1857-1874.
22. Yang, Y., et al., *REE recovery from end-of-life NdFeB permanent magnet scrap: a critical review.* J. Sustain. Metall., 2017. **3**(1): p. 122-149.
23. Rademaker, J.H., R. Kleijn, and Y. Yang, *Recycling as a strategy against rare earth element criticality: A systemic evaluation of the potential yield of NdFeB magnet recycling.* Environ. Sci. Technol., 2013. **47**(18): p. 10129-10136.
24. Habib, K. and H. Wenzel, *Exploring rare earths supply constraints for the emerging clean energy technologies and the role of recycling.* J. Clean. Prod., 2014. **84**: p. 348-359.
25. Tanaka, M., et al., *Recycling of rare earths from scrap*, in *Handbook on the physics and chemistry of rare earths*. 2013, Elsevier. p. 159-211.
26. Gorller-Walrand, C. and K. Binnemans, *Handbook on the physics and chemistry of rare earths.* North-Holland, Amsterdam, 1998: p. 123.
27. Walton, A., et al. *The use of hydrogen to separate and recycle NdeFeB magnets from electronic waste*. in *22nd International Workshop on Rare Earth Magnets and their Applications (Nagasaki, Japan)*. 2012.

28. Walton, A., et al., *The use of hydrogen to separate and recycle neodymium–iron–boron-type magnets from electronic waste.* J. Clean. Prod., 2015. **104**: p. 236-241.
29. Takeda, O. and T.H. Okabe, *Current status on resource and recycling technology for rare earths.* Metall. Mater. Trans. E, 2014. **1**(2): p. 160-173.
30. Firdaus, M., et al., *Review of high-temperature recovery of rare earth (Nd/Dy) from magnet waste.* J. Sustain. Metall., 2016. **2**(4): p. 276-295.
31. Hiskey, B., *Metallurgy, Survey.* Kirk-Othmer encyclopedia of chemical technology, 2000.
32. Habashi, F., *Recent trends in extractive metallurgy.* J. Min. Metall., Section B: Metallurgy, 2009. **45**(1): p. 1-13.
33. Bounds, C., *The recycle of sintered magnet swarf.* Metals and materials waste reduction, recovery and remediation, 1994: p. 173-186.
34. Önal, M.A.R., et al., *Hydrometallurgical recycling of NdFeB magnets: Complete leaching, iron removal and electrolysis.* J. Rare Earth., 2017. **35**(6): p. 574-584.
35. Önal, M.A.R., et al., *Recycling of NdFeB magnets using nitration, calcination and water leaching for REE recovery.* Hydrometallurgy, 2017. **167**: p. 115-123.
36. De, A.K., S.M. Khopkar, and R.A. Chalmers, *Solvent extraction of metals.* 1970.
37. Gupta, C. and N. Krishnamurthy, *Extractive metallurgy of rare earths.* Int. Mater. Rev., 1992. **37**(1): p. 197-248.
38. Thakur, N., *Separation of rare earths by solvent extraction.* Miner. Process. Extract. Metull. Rev., 2000. **21**(1-5): p. 277-306.
39. Yoon, H.-S., et al., *Solvent extraction, separation and recovery of dysprosium (Dy) and neodymium (Nd) from aqueous solutions: waste recycling strategies for permanent magnet processing.* Hydrometallurgy, 2016. **165**: p. 27-43.
40. El-Kot, A., *Solvent extraction of neodymium, europium and thulium by di-(2-ethylhexyl) phosphoric acid.* J. Radioanal. Nucl. Chem., 1993. **170**(1): p. 207-214.
41. Singh, D., M. Kotekar, and H. Singh, *Development of a solvent extraction process for production of nuclear grade dysprosium oxide from a crude concentrate.* Desalination, 2008. **232**(1-3): p. 49-58.
42. Lee, M.-S., et al., *Solvent extraction of neodymium ions from hydrochloric acid solution using PC88A and saponified PC88A.* Sep. Purif. Technol., 2005. **46**(1-2): p. 72-78.
43. Gupta, C. and N. Krishnamurthy, *Extractive metallurgy of rare earths. BR, L., NY.* 2005.
44. Hesford, E. and H. McKay, *The extraction of nitrates by tri-n-butyl phosphate (TBP). Part 3.—Extraction at trace concentrations.* Trans. Faraday Soc., 1958. **54**: p. 573-586.
45. Tyumentsev, M.S., et al., *The solvent extraction of rare earth elements from nitrate media with novel polyamides containing malonamide groups.* Hydrometallurgy, 2016. **164**: p. 24-30.
46. Dupont, D. and K. Binnemans, *Recycling of rare earths from NdFeB magnets using a combined leaching/extraction system based on the acidity and thermomorphism of the ionic liquid [Hbet][Tf2 N].* Green Chem., 2015. **17**: p. 2150-2163.
47. Riaño, S. and K. Binnemans, *Extraction and separation of neodymium and dysprosium from used NdFeB magnets: an application of ionic liquids in solvent extraction towards the recycling of magnets.* Green Chem., 2015. 17. p. 2931-2942
48. Sholl, D.S. and R.P. Lively, *Seven chemical separations: to change the world: purifying mixtures without using heat would lower global energy use, emissions and pollution and open up new routes to resources.* Nature, 2016. **532**: p. 435-438.
49. Bogart, J.A., et al., *An operationally simple method for separating the rare-earth elements neodymium and dysprosium.* Angew. Chem. Int. Edit., 2015. **54**(28): p. 8222-8225.
50. Badawy, S.M., *Uranium isotope enrichment by complexation with chelating polymer adsorbent.* Radiat. Phys. Chem., 2003. **66**(1): p. 67-71.
51. Inamuddin, L.M. and M. Luqman, *Ion exchange technology I: theory and materials.* Springer. DOI, 2012. **10**: p. 978-94.
52. Spedding, F., et al., *The separation of rare earths by ion exchange.[1,2] I. cerium and yttrium.* J. Am. Chem. Soc., 1947. **69**(11): p. 2777-2781.
53. Spedding, F., et al., *The Separation of Rare Earths by Ion Exchange.[1,2] II. Neodymium and Praseodymium.* J. Am. Chem. Soc., 1947. **69**(11): p. 2786-2792.

54. Tompkins, E.R., J.X. Khym, and W.E. Cohn, *Ion-exchange as a separations method. I. the Separation of fission-produced radioisotopes, including individual rare earths, by complexing elution from amberlite resin1*. J. Am. Chem. Soc., 1947. **69**(11): p. 2769-2777.
55. Spedding, F., et al., *The separation of rare earths by ion exchange.[1] III. pilot plant scale separations*. J. Am. Chem. Soc., 1947. **69**(11): p. 2812-2818.
56. Habashi, F., *A short history of hydrometallurgy.* Hydrometallurgy, 2005. **79**(1-2): p. 15-22.
57. Yang, P., *The chemistry of nanostructured materials*. 2003: World scientific.
58. England, W.A., et al., *Fast proton conduction in inorganic ion-exchange compounds.* Solid State Ionics, 1980. **1**(3-4): p. 231-249.
59. Roy, A.d., et al., *Expanded clays and other microporous solids*. 1992, Van Nostrand Reinhold, New York. p. 108-169.
60. Behrens, E.A., D.M. Poojary, and A. Clearfield, *Syntheses, crystal structures, and ion-exchange properties of porous titanosilicates, $HM_3Ti_4O_4(SiO_4)_3{\cdot}4H_2O$ ($M= H^+, K^+, Cs^+$), Structural analogues of the mineral pharmacosiderite.* Chem. Mater., 1996. **8**(6): p. 1236-1244.
61. Yin, Y.-G., et al., *Studies of oxygen species in synthetic todorokite-like manganese oxide octahedral molecular sieves.* Chem. Mater., 1994. **6**(10): p. 1803-1808.
62. Boeyens, J., G.J. McDougal, and J.V.R. Smit, *Crystallographic study of the ammonium/potassium 12-molybdophosphate ion-exchange system.* J. Solid State Chem., 1976. **18**(2): p. 191-199.
63. Vivani, R., et al., *New advances in zirconium phosphate and phosphonate chemistry: Structural archetypes.* Microporous Mesoporous Mater., 2008. **107**(1): p. 58-70.
64. Lehto, J. and R. Harjula, *Selective separation of radionuclides from nuclear waste solutions with inorganic ion exchangers.* Radiochim. Acta, 1999. **86**(1-2): p. 65-70.
65. Emig, G. and H. Hofmann, *Action of zirconium phosphate as a catalyst for the oxydehydrogenation of ethylbenzene to styrene.* J. Catal., 1983. **84**(1): p. 15-26.
66. Rao, K.N., et al., *Zirconium phosphate supported tungsten oxide solid acid catalysts for the esterification of palmitic acid.* Green Chem., 2006. **8**(9): p. 790-797.
67. Clearfield, A., *Inorganic ion exchangers with layered structures.* Annu. Rev. Mater. Sci., 1984. **14**(1): p. 205-229.
68. Clearfield, A. and J. Troup, *Mechanism of ion exchange in crystalline zirconium phosphate. II. Lithium ion exchange of. alpha.-zirconium phosphate.* J. Phys. Chem., 1970. **74**(2): p. 314-317.
69. Clearfield, A., et al., *Mechanism of ion exchange in crystalline zirconium phosphates. I. sodium ion exchange of alpha-zirconium phosphate.* J. Phys. Chem., 1969. **73**(10): p. 3424-3430.
70. Clearfield, A., et al., *On the mechanism of ion exchange in crystalline zirconium phosphates-IV potassium ion exchange of α-zirconium phosphate.* J. Inorg. Nucl. Chem., 1972. **34**(1): p. 329-337.
71. Clearfield, A. and R.M. Tindwa, *On the mechanism of ion exchange in zirconium phosphates—XXI intercalation of amines by α-zirconium phosphate.* J. Inorg. Nucl. Chem., 1979. **41**(6): p. 871-878.
72. Hattori, T., A. Ishiguro, and Y. Murakami, *Acidity of crystalline zirconium phosphate.* J. Inorg. Nucl. Chem., 1978. **40**(6): p. 1107-1111.
73. Keller, S.W., H.-N. Kim, and T.E. Mallouk, *Layer-by-layer assembly of intercalation compounds and heterostructures on surfaces: toward molecular" beaker" epitaxy.* J. Am. Chem. Soc., 1994. **116**(19): p. 8817-8818.
74. Díaz, A., et al., *Zirconium phosphate nano-platelets: a novel platform for drug delivery in cancer therapy.* Chem. Commun., 2012. **48**(12): p. 1754-1756.
75. Rodriguez-Castellon, E., A. Rodriguez-Garcia, and S. Bruque, *Intercalation of polar organic compounds into tin(IV) hydrogenphosphate monohydrate.* Inorg. Chem., 1985. **24**(8): p. 1187-1190.
76. Harvie, S.J. and G.H. Nancollas, *Ion exchange properties of crystalline zirconium phosphate.* J. Inorg. Nucl. Chem., 1970. **32**(12): p. 3923-3937.
77. Clearfield, A. and J. Stynes, *The preparation of crystalline zirconium phosphate and some observations on its ion exchange behaviour.* J. Inorg. Nucl. Chem., 1964. **26**(1): p. 117-129.
78. Clearfield, A., *Inorganic ion exchangers, past, present, and future.* Solvent Extr. Ion Exc, 2000. **18**(4): p. 655-678.
79. Sun, L., et al., *Preparation of α-zirconium phosphate nanoplatelets with wide variations in aspect ratios.* New J. Chem., 2007. **31**(1): p. 39-43.

80. Clearfield, A., A. Oskarsson, and C. Oskarsson, *On the mechanism of ion exchange in crystalline zirconium phosphates. VI. The effect of crystallinity of the exchanger on Na^+/H^+ exchange.* Ion exch. Membr., 1972. **1**(2): p. 91-107.
81. Trobajo, C., et al., *On the synthesis of α-zirconium phosphate.* Chem. Mater., 2000. **12**(6): p. 1787-1790.
82. Sydorchuk, V., et al., *Synthesis, structure and some properties of zirconium phosphate/oxide support compositions*. J. Therm. Anal. Calorim., 2011. **108**(3): p. 1009-1016.
83. Khalameida, S., et al., *Hydrothermal, microwave and mechanochemical modification of amorphous zirconium phosphate structure.* J. Therm. Anal. Calorim., 2017. **128**(2): p. 795-806.
84. Dyer, A., T. Shaheen, and M. Zamin, *Ion exchange of strontium and caesium into amorphous zirconium phosphates*. J. Mater. Chem., 1997. **7**(9): p. 1895-1899.
85. Zhang, Q., et al., *Rationally designed porous polystyrene encapsulated zirconium phosphate nanocomposite for highly efficient fluoride uptake in waters.* Sci. Rep., 2013. **3**: p. 1-9.
86. Zhang, Q., et al., *Selective sorption of lead, cadmium and zinc ions by a polymeric cation exchanger containing nano-Zr $(HPO_3S)_2$.* Environ. Sci. Technol., 2008. **42**(11): p. 4140-4145.
87. Ma, F., et al., *Preparation, characterization and ion-exchange behavior of polyantimonic acid-polyacrylonitrile (PAA–PAN) composite beads for strontium(II).* J. Radioanal. Nucl. Chem., 2016. **308**(1): p. 155-163.
88. Griffith, C.S., et al., *Separation of cesium and strontium from acidic radioactive waste simulants using a microporous tungstate/polyacrylonitrile (PAN) composite adsorbent.* Sep. sci. technol., 2005. **40**(9): p. 1781-1796.
89. Padungthon, S., et al., *Polymeric anion exchanger supported hydrated Zr(IV) oxide nanoparticles: a reusable hybrid sorbent for selective trace arsenic removal.* React. Funct. Polym., 2015. **93**: p. 84-94.
90. Geng, Z., et al., *Highly efficient dye adsorption and removal: a functional hybrid of reduced graphene oxide–Fe_3O_4 nanoparticles as an easily regenerative adsorbent.* J. Mater. Chem., 2012. **22**(8): p. 3527-3535.
91. Yin, M., et al., *Magnetic self-assembled zeolite clusters for sensitive detection and rapid removal of mercury (II).* ACS Appl. Mater. Inter., 2011. **4**(1): p. 431-437.
92. Caliskan, N., et al., *Adsorption of zinc (II) on diatomite and manganese-oxide-modified diatomite: A kinetic and equilibrium study.* J. Hazard. Mater., 2011. **193**: p. 27-36.
93. Liu, Z., et al., *Magnetic cellulose–chitosan hydrogels prepared from ionic liquids as reusable adsorbent for removal of heavy metal ions.* Chem. Commun., 2012. **48**(59): p. 7350-7352.
94. Dwivedi, C., et al., *Copper hexacyanoferrate–polymer composite beads for cesium ion removal: Synthesis, characterization, sorption, and kinetic studies.* J Appl. Polym. Sci., 2013. **129**(1): p. 152-160.
95. Wang, H.C., et al., *Mesoporous silica particles integrated with all–inorganic $CsPbBr_3$ perovskite quantum–dot nanocomposites (MP–PQDs) with high stability and wide color gamut used for backlight display.* Angew. Chem. Int. Edit., 2016. **55**(28): p. 7924-7929.
96. Sebesta, F. and J. John, *An overview of the development, testing, and application of composite absorbers*. 1995, Los Alamos National Lab., NM (United States).
97. Sebesta, F., J. John, and A. Motl, *Development of composite ion exchangers and their use in treatment of liquid radioactive wastes.* Waste Treatment and Immobilization Technologies Involving Inorganic Sorbents, IAEA-TECDOC-947, IAEA, Vienna, 1997: p. 79-103.
98. İnan, S. and Y. Altaş, *Preparation of zirconium–manganese oxide/polyacrylonitrile (Zr–Mn oxide/PAN) composite spheres and the investigation of Sr(II) sorption by experimental design.* Chem. Eng. J., 2011. **168**(3): p. 1263-1271.
99. İnan, S., R. Koivula, and R. Harjula, *Removal of ^{63}Ni and ^{57}Co from aqueous solution using antimony doped tin dioxide–polyacrylonitrile (Sb doped SnO_2–PAN) composite ion-exchangers.* J. Radioanal. Nucl. Chem., 2014. **299**(1): p. 901-908.
100. Moon, J.-K., et al., *Preparation of organic-inorganic composite adsorbent beads for removal of radionuclides and heavy metal ions.* J. Radioanal. Nucl. Chem., 2000. **246**(2): p. 299-307.
101. Moon, J.-K., et al., *Preparation of PAN-zeolite 4A composite ion exchanger and its uptake behavior for Sr and Cs ions in acid solution.* Korean J. Chem. Eng., 2002. **19**(5): p. 838-842.

102. Rajeh, A. and L. Szirtes, *Investigations of crystalline structure of gamma-zirconium phosphate.* J. Radioanal. Nucl. Chem., 1995. **196**(2): p. 319-322.
103. Krogh Andersen, A.M., et al., *Preparation and characterization of a new 3-dimensional zirconium hydrogen phosphate, τ-Zr(HPO$_4$)$_2$. Determination of the complete crystal structure combining synchrotron X-ray single-crystal diffraction and neutron powder diffraction.* Inorg. chem., 1998. **37**(5): p. 876-881.
104. Clearfield, A., *Inorganic ion exchange materials*. 1982: CRC press.
105. Corma, A., *Solid acid catalysts.* Curr Opin Solid St. M., 1997. **2**(1): p. 63-75.
106. Sharygin, L., et al., *Synthesis of zirconium,titanium and tin phosphates by sol-gel method and study of their properties.* Izv. Akad. Nauk SSSR, Neorg. Mater, 1983. **19**(11): p. 1899-1902.
107. Mosby, B.M., et al., *Surface functionalization of zirconium phosphate nanoplatelets for the design of polymer fillers.* ACS Appl. Mater. Interfaces, 2013. **6**(1): p. 585-592.
108. Jones, D.J., et al., *Incoherent inelastic neutron scattering studies of proton-conducting materials: Sn (HPO$_4$)$_2$· H$_2$O and HM (SO$_4$)$_2$· H$_2$O, M= Fe, In: Part II. The vibrational spectrum of H$_3$O$^+$.* J. Mol. Struct., 1989. **197**: p. 113-121.
109. Hudson, M.J. and A.D. Workman, *High-resolution solid-state ^{31}P and ^{119}Sn magic-angle spinning nuclear magnetic resonance studies of amorphous and microcrystalline layered metal (IV) hydrogenphosphates.* J. Mater. Chem., 1991. **1**(3): p. 375-379.
110. Bortun, A.I., et al., *Synthesis and characterization of ion exchange properties of spherically granulated titanium phosphate.* Solvent Extra. Ion Exch., 1997. **15**(3): p. 515-532.
111. Samed, A.J., et al., *Synthesis of ZrP$_2$O$_7$ by hydrothermal reaction and post-calcination.* J. Ceram. Soc. Jpn. , 2011. **119**: p. 81-84.
112. Behrendt, D., K. Beneke, and G. Lagaly, *Intercalation compounds of zirconium phosphate.* Angew. Chem. Int. Edit., 1976. **15**(9): p. 544-545.
113. Horsley, S., D. Nowell, and D. Stewart, *The infrared and Raman spectra of α-zirconium phosphate.* Spectrochim. Acta. A: Mol. Spectrosc., 1974. **30**(2): p. 535-541.
114. Helfferich, F., *Ion Exchange.− New York*. 1995, Dover.
115. García-Glez, J., et al., *α-Titanium phosphate intercalated with propylamine: an alternative pathway for efficient europium(III) uptake into layered tetravalent metal phosphates.* Arab. J. Chem., 2017. **10**(6): p. 885-894.
116. Gustafsson, J.P., *Visual minteq.* Capturado em de, 2006. **26**.
117. Cheung, W., Y. Szeto, and G. McKay, *Intraparticle diffusion processes during acid dye adsorption onto chitosan.* Bioresource technol., 2007. **98**(15): p. 2897-2904.
118. Ho, Y.-S. and G. McKay, *Pseudo-second order model for sorption processes.* Process Biochem., 1999. **34**(5): p. 451-465.
119. Lee, G.S., et al., *Distribution coefficients of La, Ce, Pr, Nd, and Sm on Cyanex 923, D2EHPA, and PC88A impregnated resins.* Sep. Purif. Technol., 2009. **67**(1): p. 79-85.
120. Zheng, X., et al., *Design of mesoporous silica hybrid materials as sorbents for the selective recovery of rare earth metals.* J. Mater. Chem. A, 2015. **3**(19): p. 10327-10335.
121. Nightingale Jr, E., *Phenomenological theory of ion solvation. Effective radii of hydrated ions.* J. Phys. Chem., 1959. **63**(9): p. 1381-1387.
122. Lundqvist, R., E. Hulet, and P. Baisden, *Electromigration method in tracer studies of complex chemistry. 2.* Acta Chem. Scand., Ser. A, 1981. **35**(9): p. 653-661.
123. Jandera, P. and J. Churacek, *Gradient elution in column liquid chromatography: theory and practice*. Vol. 31. 1985: Elsevier.
124. Vander Hoogerstraete, T., et al., *From NdFeB magnets towards the rare-earth oxides: a recycling process consuming only oxalic acid.* RSC Adv., 2014. **4**(109): p. 64099-64111.
125. Jenkins, R. and R.L. Snyder, *Diffraction theory*. 2012: Wiley Online Library.
126. Griffiths, P.R. and J.A. De Haseth, *Fourier transform infrared spectrometry*. Vol. 171. 2007: John Wiley & Sons.
127. Gabbott, P., *Principles and applications of thermal analysis*. 2008: John Wiley & Sons.
128. Perez, J.R., et al., *Image-guided fluorescence endomicroscopy: from macro-to micro-imaging of radiation-induced pulmonary fibrosis.* Sci. Rep., 2017. **7**: p. 1-11.